Separation of Molybdenum and Copper in Porphyry Deposits

The Roles of Sulfur, Redox, and pH in Ore Mineral Deposition at Bingham Canyon

Originally published in:
Economic Geology 107(2), https://doi.org/10.2113/econgeo.107.2.333

This is the green Open Access version of: Seo, J. H., Guillong, M. and Heinich, C. A., 2012. Seperation of Molybdenum and Copper in Porphyry Deposits: The Roles of Sulfur, Redox and pH in Ore Mineral Deposition at Bingham Canyon. *Economic Geology,* vol. 107, pp. 333-356.
https://doi.org/10.2113/econgeo.107.2.333

Separation of Molybdenum and Copper in Porphyry Deposits: The Roles of Sulfur, Redox and pH in Ore Mineral Deposition at Bingham Canyon

Jung Hun Seo[1], Marcel Guillong[1,*], Christoph A. Heinrich[1,2]

[1]Department of Earth Sciences, ETH Zurich, 8092 Zurich, Switzerland
[2]Faculty of Mathematics and Natural Sciences, University of Zurich, Switzerland

* Corresponding author: e-mail, seo28@snu.ac.kr

Jung Hun SEO (seo@erdw.ethz.ch), Marcel GUILLONG (Marcel.Guillong@utas.edu.au), Christoph A. HEINRICH (heinrich@erdw.ethz.ch)

Keywords: Molybdenum, Sulfur, Copper, Fluid inclusion, Porphyry deposit

Abstract

The giant Bingham Canyon porphyry Cu-Mo-Au deposit (Utah) is associated with Eocene subvolcanic intrusions. It shows a distinct metal zonation above a barren core, with 1) dominantly shallow Cu-Au mineralization (Cu-stage) following the early Quartz Monzonite Porphyry (QMP) intrusion and 2) spatially deeper Mo mineralization (Mo-stage) occurring in a separate vein set exclusively after a late Quartz Latite Porphyry (QLP) intrusion that truncates earlier Cu-Au veins. To understand this metal separation and the geochemical process of molybdenite mineralization, we investigated fluid inclusions by microthermometry, Raman spectroscopy and laser ablation inductively couple plasma mass spectrometry (LA-ICP-MS) microanalysis in low-grade and high-grade quartz veins of both mineralization stages.

In deep, low-grade quartz veins interpreted to represent the root zone of the Cu-stage we found high concentrations of Cu, S, and Mo in the fluid inclusions, whereas in low-grade Mo-stage veins, we found lower Cu, but similar concentrations of S and Mo, compared to the inferred input fluids to the Cu-stage. Sulfur and copper concentrations were similar in intermediate-density (ID) type fluid inclusions in deep low-grade Cu-stage samples, whereas ID-type inclusions in low-grade Mo-stage veins have S contents that exceed their Cu contents. In high-grade Mo-stage vein, we found large variations of Mo concentrations in coexisting brine and vapor inclusions. Compared to the P-T conditions of the Cu-precipitation stage (90-260 bars and 320-430 °C), the Mo-precipitating fluids were trapped at higher pressures and temperatures of 140-710 bars and 360-580 °C. Mass-balance calculation based on the compositions of ID inclusions and brine + vapor assemblages, interpreted to be derived by phase separation during decompression of the ascending

single-phase ID fluid, indicate that the mass of vapor phase exceeded that of brine by about 9:1 in both mineralization stages. Combining this mass-balance with the analyzed vapor/brine partitioning data indicates that more than 70% of Mo, and S (by mass) in the deposit were deposited from the vapor phase. Earlier Cu-Au deposition was similarly dominated by vapor, but recently published data about post-entrapment Cu diffusion in and out of fluid inclusions cast doubt on previous quantifications suggesting that almost none of the copper was deposited by brine.

Mo is less likely to be modified by selective diffusion, and high Mo contents (max. 0.0054 Mo/Na in ID; 380 µg/g Mo in brine) in the hydrothermal fluids were maintained from the early Cu-stage to the late Mo-stage. This indicates that Mo concentration was not the decisive factor for separate precipitation of late Mo ore at Bingham Canyon. Instead, the metal separation may be explained by a reduction in redox potential and an increase in acidity in the evolving source region of the fluids, i.e., a large subvolcanic magma reservoir. This is indicated by the stoichiometry of chalcopyrite and molybdenite precipitation reactions, a tentative difference in the Fe/Mn ratio in fluids of both veining stages, incipient muscovite alteration along high-temperature molybdenite veins and an increasing tendency for Mo to fractionate from brine to vapor. We suggest that the early Cu-stage fluids were slightly more oxidized and neutral, allowing Cu-Fe sulfides to saturate first, while molybdenite saturation was suppressed and Mo was lost from the early ore stage. By contrast during the later Mo-stage, the fluids were more reduced and acidic, thereby allowing selective saturation of molybdenite as the first precipitating sulfide in the cooling and expanding two-phase fluid, consistent with textural observations. This interpretation may imply more generally that small differences in redox potential and acid/base balance of the magmatic source of porphyry-mineralizing systems may be decisive in the temporal and spatial separation of the two metals.

Introduction

Porphyry-style deposits are the most important Cu and Mo inventories in the world economically (Singer et al., 2005). Among porphyry-style deposits, most polymetallic Cu-Mo-Au deposits are associated with compositionally intermediate (e.g. granodiorite, quartz monzonite) subvolcanic intrusions (Beane and Titley, 1981), whereas Mo-only porphyry deposits (Climax-type) are associated with high-silica rhyolite magma intrusions (White et al., 1981). In porphyry deposits that contain Mo as well as Cu, paragenetic relationships of molybdenite and Cu sulfides from the vein to the orebody scale commonly indicate that molybdenite deposition postdates the main stage of precipitation of Cu-Fe sulfides ± Au (Gustafson and Hunt, 1975; Ulrich and Heinrich, 2001; Rusk et al., 2008; Landtwing et al., 2010; Redmond and Einaudi, 2010; Sillitoe, 2010).

Metal ratios including Cu/Au and Mo/Cu and molybdenite grades are of economic importance, but the geological causes for their variation are not clearly established. The Cu/Au ratios in porphyry-style deposits suggested to be influenced by a combination of processes including (1) magma compositions, such as alkaline affinity, redox state, and sulfide melt incorporation (Sillitoe, 1997; Ulrich et al., 1999; Halter et al., 2002; Heinrich et al., 2004; Zajacz et al., 2010), (2) the depth of emplacement affecting the extent of phase separations of magmatic-hydrothermal fluids and metal partitioning (Simon et al., 2006), explaining why most Au-rich porphyries are relatively shallow (Cox and Singer, 1988; Sillitoe, 1997; Landtwing et al., 2010; Murakami et al., 2010), and (3) a mineralogical control on selective extraction of Au from fluid into Cu-Fe-sulfide solid solutions, notably bornite (Simon et al., 2000; Kesler et al., 2002).

The factors controlling the Mo/Cu ratio and the molybdenite grade in porphyry Cu-Mo-Au deposits remain even more elusive. The Mo grades in some deposits show a rough

correlation with formation depth, i.e., deep porphyry deposits tend to be Au-poor but commonly have high Mo grades, such as Butte, Montana (Singer et al., 2005; Rusk et al., 2008; Murakami et al., 2010). Provinciality and large-scale source processes are indicated by the clustering of the world's largest Mo-rich and Mo-only porphyry deposits in the SW-USA, including Bingham Canyon, Butte, Climax, Henderson, and Questa (Singer et al., 2005). Recent study of Pb isotopes in rocks and ore-forming fluids suggested that the Mo-mineralizing magmas of this province were produced by melting of ancient subcontinental lithospheric mantle affected by ancient Proterozoic rather than coeval subduction metasomatism (Pettke et al., 2010). The compositional evolution of fluids that formed the Mo-only deposit of Questa showed that their source magmas must have experienced extensive batholith-scale or lower-crustal fractionation (Audétat and Pettke, 2003; Klemm et al., 2008), which may contribute to enrichment of incompatible Mo in residual fluids and explain the typical association Mo-only porphyries with very fractionated magmas (White et al., 1981; Wallace, 1995; Seedorff and Einaudi, 2004a; Audétat, 2010). Additional to a magmatic source control, selective precipitation of molybdenite from the magmatic-hydrothermal fluids in Mo-rich deposits could be an important factor in metal separation. LA-ICP-MS microanalyses of the fluid inclusions in the Questa deposit showed that the magmatic-hydrothermal fluids contain more Cu than Mo, although molybdenite was deposited without significant Cu sulfides (Klemm et al., 2008). High Mo concentrations in brine inclusion assemblages supported the interpretation that MoS_2 was dominantly precipitated from brine, whereas Cu was selectively distilled away from the region of the present Questa orebody by an ascending vapor phase fluid (Klemm et al., 2008).

From hydrothermal experiments, molybdic acid species such as H_2MoO_4 were suggested to be important for Mo transport in high-temperature hydrothermal fluids (Candela and Holland, 1984; Keppler and Wyllie, 1991; Rempel et al., 2006; Rempel et al., 2008; Minubayeva and Seward, 2010). While high Mo solubilities up to 1.6 wt% were reported in sulfur-free saline solutions (Ulrich and Mavrogenes, 2008), much lower Mo solubilities (less than 1 ppm) were reported in sulfur-bearing multicomponent solubility experiments (Wood et al., 1987; Cao, 1989; Gu, 1993). Sulfur limits hydrothermal Mo mobility through the saturation of molybdenite as a primary magmatic accessory mineral (Bingen and Stein, 2003). Sulfur is an essential element for economically significant precipitation of molybdenite (MoS_2) from hydrothermal fluids. With the recent analytical advances of quantifying S in single quartz-hosted fluid inclusions by laser ablation inductively coupled plasma mass spectrometry (LA-ICP-MS) (Guillong et al., 2008a; Seo et al., 2011), we showed that magmatic-hydrothermal fluids contain enough sulfur to precipitate sulfide minerals (e.g. $CuFeS_2$ and MoS_2), but that the concentrations of S and major chalcophile elements (Cu, Fe) are commonly of similar magnitude (Seo et al., 2009). This opens the possibility that competition between metals and sulfur could be a limiting factor in ore deposition and may contribute to the large-scale separation of metals into distinct ore types (Heinrich, 2006).

The Bingham Canyon porphyry Cu-Mo-Au deposit is particularly suitable for comparing the mechanisms of copper sulfide and molybdenite precipitation because it records temporally well-separated hydrothermal stages of early Cu-Au and late Mo mineralization. The molybdenite-bearing quartz veins were formed exclusively after quartz latite porphyry (QLP) dike intrusions, whereas most Cu-Au mineralizing quartz veins predated these dikes (Redmond and Einaudi, 2010). Recent publications on the physical and chemical evolution of the giant Bingham Canyon ore system (Gruen et al., 2010; Landtwing et al., 2010; Redmond and Einaudi, 2010) provide a framework to compare the sulfur, copper, and molybdenum concentrations in fluid inclusion assemblages both from early Cu-Au-sulfide (Cu-stage) and late molybdenite-bearing (Mo-stage) quartz veins, with the aim of

understanding the factors that led to the separation of molybdenite from copper sulfides and gold.

Geology and Sampling Strategy

Geological background of the Bingham Canyon deposit

The Bingham Canyon Cu-Mo-Au deposit is hosted by series of Late Eocene subvolcanic monzonitic intrusions (collectively called the Bingham Stock) emplaced into Paleozoic sedimentary formations consisting of quartzite and limestone. The Bingham Stock is made up of four main intrusions (Redmond and Einaudi, 2010). The Equigranular Monzonite (EM) is the oldest phase of the Bingham Stock, which did not produce any mineralized veins. The EM was intruded by Quartz Monzonite Porphyry (QMP) followed by the most intense Cu-Au mineralization (Cu-stage). After the QMP, intrusion of Latite Porphyry (LP) and Quartz Latite Porphyry (QLP) dikes followed (EM → QMP → LP → QLP). The major Mo-stage mineralization postdated the QLP intrusion (Gruen et al., 2010; Landtwing et al., 2010; Redmond and Einaudi, 2010).

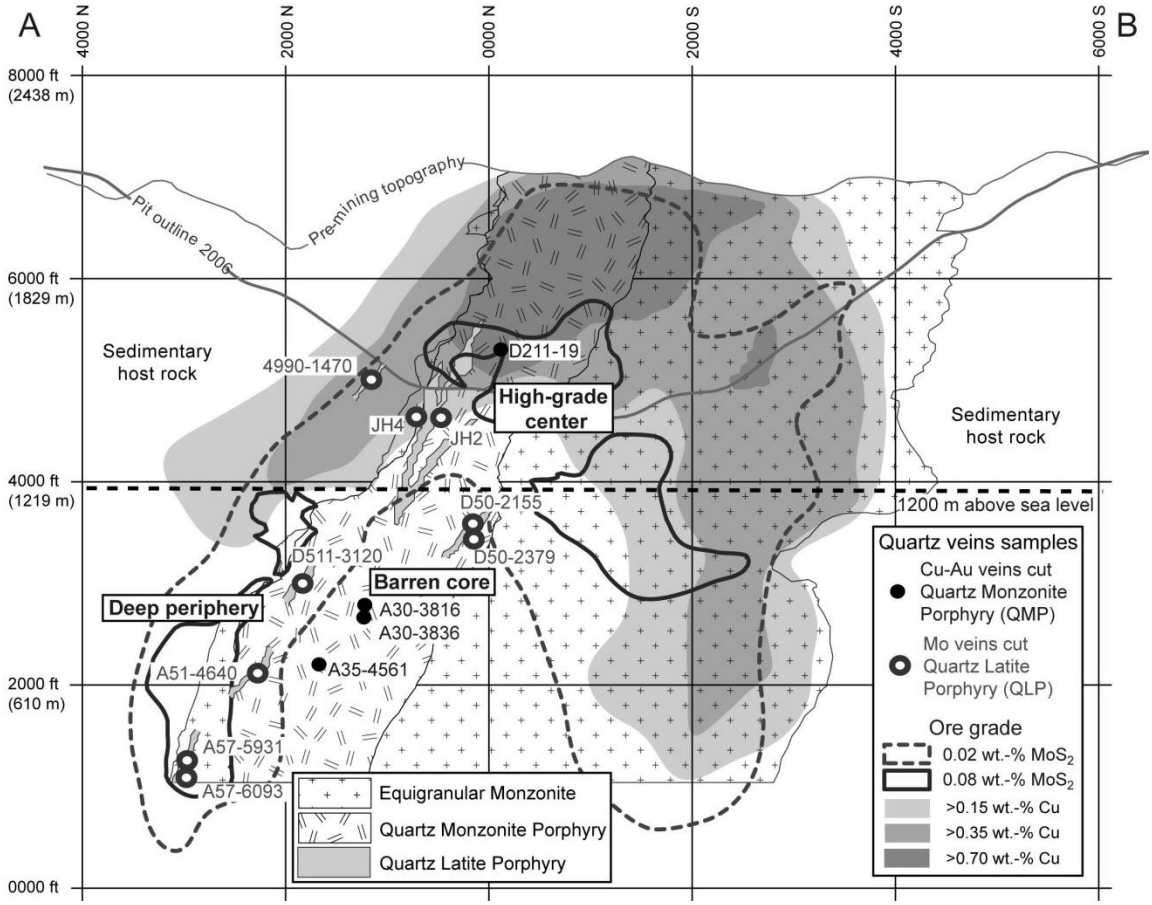

Figure 1. Northwest-southeast cross section through Bingham Canyon (refer to A-B in Fig.7 of Gruen et al., 2010 for section location) showing lithologies of the Bingham Stock, Cu and MoS_2 ore grade contours, and locations of quartz vein samples with respect to the sampling regions discussed in the text. The Cu- stage quartz stockwork veins were sampled from quartz monzonite porphyry (QMP) and late-stage quartz latite porphyry (QLP) dikes (sample 4990-1470), whereas all Mo-stage quartz-molybdenite veins were sampled from quartz latite porphyry. Samples A30-3816, 3836 (Cu-stage) and D50-2155, 2379 (Mo-stage) are from the barren core (elevation below 1,200 m). Samples D211-19 (Cu-stage), JH2, JH4 (Mo-stage), and 4990-1470 (post-QLP Cu-stage and Mo-stage) are from the high-grade center (elevation greater than 1,200 m). Samples A57-5931, 6093, A51-4640, and D511-3120 (Mo-stage) are from the deep periphery of the deposit (elevation below 1,200 m).

The Cu-rich (contour of 0.15 wt% of Cu) ore body at Bingham Canyon deposit is bell-shaped. The central highest-grade Cu ore body (> 0.70 wt% of Cu) additionally contains high Au grades (contours of 0.30 and 1.00 ppm of Au; Fig. 1; Gruen et al., 2010; Landtwing et al., 2010). Molybdenite is concentrated deeper and inward compared to Cu-Au mineralization, but the shape of the Mo-rich ore zone (contour of 0.08 wt% MoS_2) resembles that of the Cu-rich shell (Fig. 1). While the highest-grade Cu accumulated around the central part of the mine, high grade Mo (contour of 0.02 wt% MoS_2) zones are more broadly distributed from the central to the peripheral part. At the top of the deposit, the center of the high grade Mo-rich zone partially overlaps with that of the high-grade Cu zone (0.70 wt% Cu) (Fig. 1).

Copper-gold mineralization without any discernable molybdenite is associated with quartz stockwork veining and pervasive potassic alteration. Most Cu-Au stage stockwork veins are contemporaneous with or postdate the intrusion of Quartz Monzonite Porphyry (Fig. 2) but stockwork veining with diminishing intensity followed the intrusion of Latite Porphyry and Quartz Latite Porphyry. Molybdenite mineralization of a distinct Mo-stage formed typically 10-60 mm thick quartz-molybdenite veins. Theses veins consistently postdate the late intrusion of Quartz Latite Porphyry wherever we checked areas of economic Mo grades that also contain the Quartz Latite Porphyry dikes. These quartz-molybdenite veins typically contain euhedral and partly free-standing quartz crystals (3-2 in Fig. 2). In the vuggy center of the quartz-molybdenite veins, minor late chalcopyrite is precipitated as euhedral crystals (3-2 in Fig. 2B and Fig. 2C), locally overgrown by calcite. Most quartz-molybdenite veins occur in areas of pervasive biotite alteration, which may at least in part be related to earlier Cu-Au stage stockwork veining and its barren core. At least locally, previously weakly altered wall rocks next to quartz-molybdenite veins show a bleached halo containing fine-grained muscovite (Fig. 2C). All generations of quartz Cu-Au stockwork veins and the late quartz-molybdenite veins have been cut by quartz-pyrite (±chalcopyrite ± calcite) veins with broad haloes of feldspar-destructive alteration (sericite ± clay minerals; QSP veins) (Redmond and Einaudi, 2010).

Sample descriptions

We sampled quartz veins of three paragenetic stages that show clear and consistent time sequences of emplacement in drill core and in outcrop: (1) *Quartz stockwork veins* associated with the main Cu-Au mineralization, hosted by QMP and early EM, (2) *late-stage quartz stockwork veins* that clearly postdate the latest QLP dikes and are associated with minor late copper mineralization, and (3) *quartz-molybdenite veins* that consistently postdate QLP at each sampling site and also cut the late stockwork veins where present. We sampled these vein generations in the low grade center of the deposit (*barren core*), in deep Mo-rich peripheral zone accessible in drill core only (*deep periphery*), and in the high-grade Cu-Au and Mo rich center of the open pit (*high-grade center*; Fig. 1). From a greater number of reconnaissance samples, 13 veins were studied in detail, to obtain textural information and quantitative data from 115 fluid inclusion assemblages comprising 3 to 10 individual inclusions each (Table 1, 2, 3, 4).

Deep quartz stockwork veins (Cu-stage in barren core; A30-3816, 3836, and A35-4561) are located lower than 1,200 m above sea level in the center of the mine. They contain minor amounts of disseminated pyrite and chalcopyrite in potassically altered QMP. Based on mineralogy and similar textural appearance (variably irregular, sugary-texture without vugs), these deep quartz stockwork veins were interpreted to be the channelways of fluids generating the main Cu-Au stage mineralization in the higher part of the system (Landtwing et al., 2010). These veins usually contain three types of fluid inclusions: predominant CO_2-bearing intermediate-density fluid inclusions, and less abundant vapor and brine inclusions (Redmond et al., 2004). A high-grade Cu-Au quartz stockwork vein (D211-19) hosted by K-

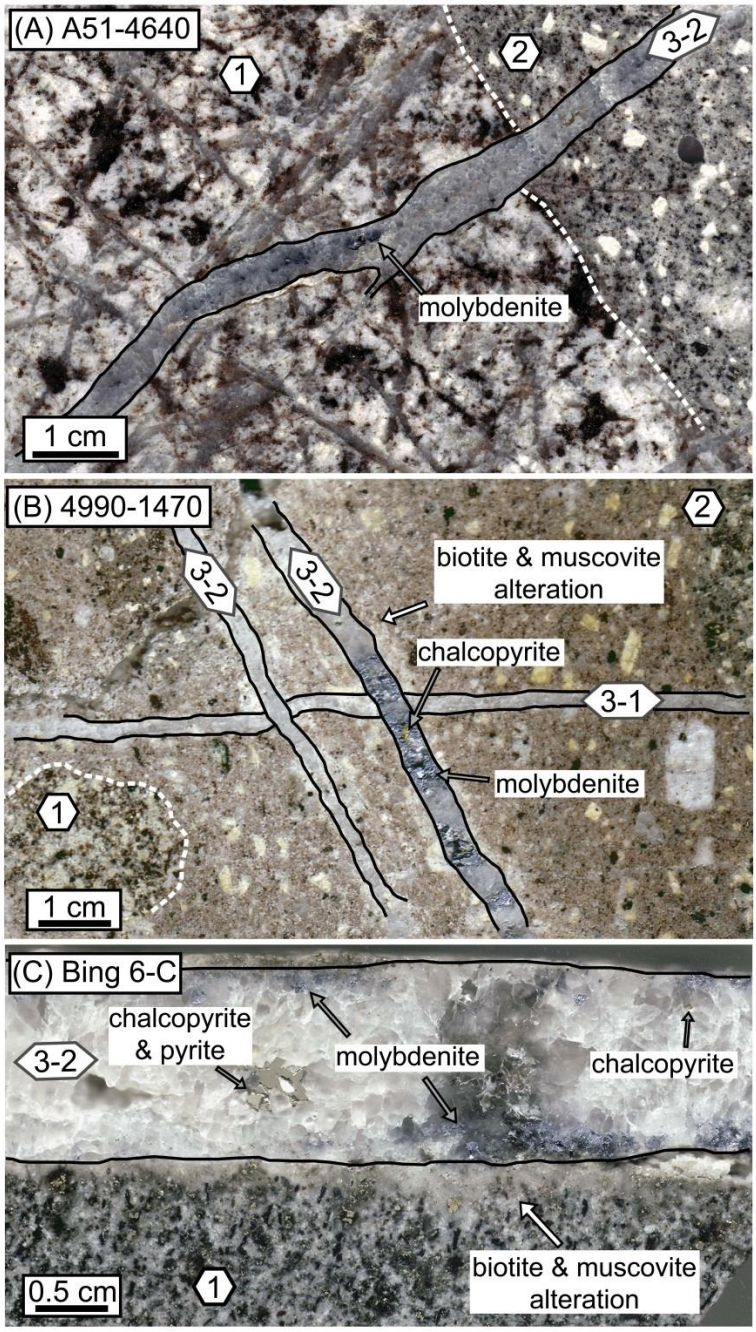

Figure 2. Photograph of polished slabs showing temporal relationships between intrusions, quartz veins, and alteration assemblages. (**A**) Quartz Monzonite Porphyry (1) has been cut first by quartz stockwork veinlets, then intruded by Quartz Latite Porphyry (2) and finally cut by a quartz-molybdenite vein (3-2) (deep periphery, A51-4640), (**B**) Quartz Latite Porphyry (2) with quartz stockwork veined Quartz Monzonite Porphyry clasts (1) is cut by a late quartz stockwork vein (3-1) and quartz molybdenite veins (3-2) (shallow peripheral/central zone, 4990-1470). (**C**) Quartz-molybdenite vein is hosted in Quartz Monzonite Porphyry (1) (high-grade center, Bing 6-C).

The Quartz Monzonite Porphyry intrusion with pervasive potassic alteration introduced by abundant quartz stockwork veining (1) which predates the Quartz Latite Porphyry dike (2), and quartz-molybdenite vein crosscut the previous intrusions and veins (3-2). Cu-bearing late-stage quartz stockwork vein (3-1) hosted in late Quartz Latite Porphyry dike (2) and the vein is cut by vuggy quartz-molybdenite vein (3-2). Late euhedral chalcopyrite occur at the centerline of some quartz-molybdenite veins (e. g. 3-2 in B and C). Biotite and muscovite alteration halos occur quartz-molybdenite veins. White dashed line represent contact of Quartz Monzonite Porphyry - Quartz Latite Porphyry and black solid line represent quartz veins.

feldspar and biotite altered QMP comes from the center of the deposit at 1,600 m above sea level. Its blocky quartz grains contain chalcopyrite and bornite precipitated at an interstitial paragenetic position between an early re-dissolved and a later re-cementing generation of vein quartz (Landtwing et al., 2005; Landtwing et al., 2010). The high-grade quartz vein contains predominantly vapor and brine inclusions that are partly trapped on single healed microfractures as cogenetic vapor and brine (boiling assemblage).

Although most Cu-bearing quartz stockwork veins formed before the QLP intrusion, late-stage quartz stockwork veins of otherwise similar appearance cut the QLP intrusion and contain a minor amount of Cu minerals (post-QLP Cu-stage; 3-1 in Fig. 2B), including bornite and digenite. These late-stage quartz stockwork veins are usually less than 10 mm wide and have been crosscut by high-grade quartz molybdenite veins (3-2 in Fig. 2B). Fluid inclusion types in the late-stage QLP-hosted quartz stockwork vein are mostly vapor and brine inclusions, locally as cogenetic vapor+brine pairs.

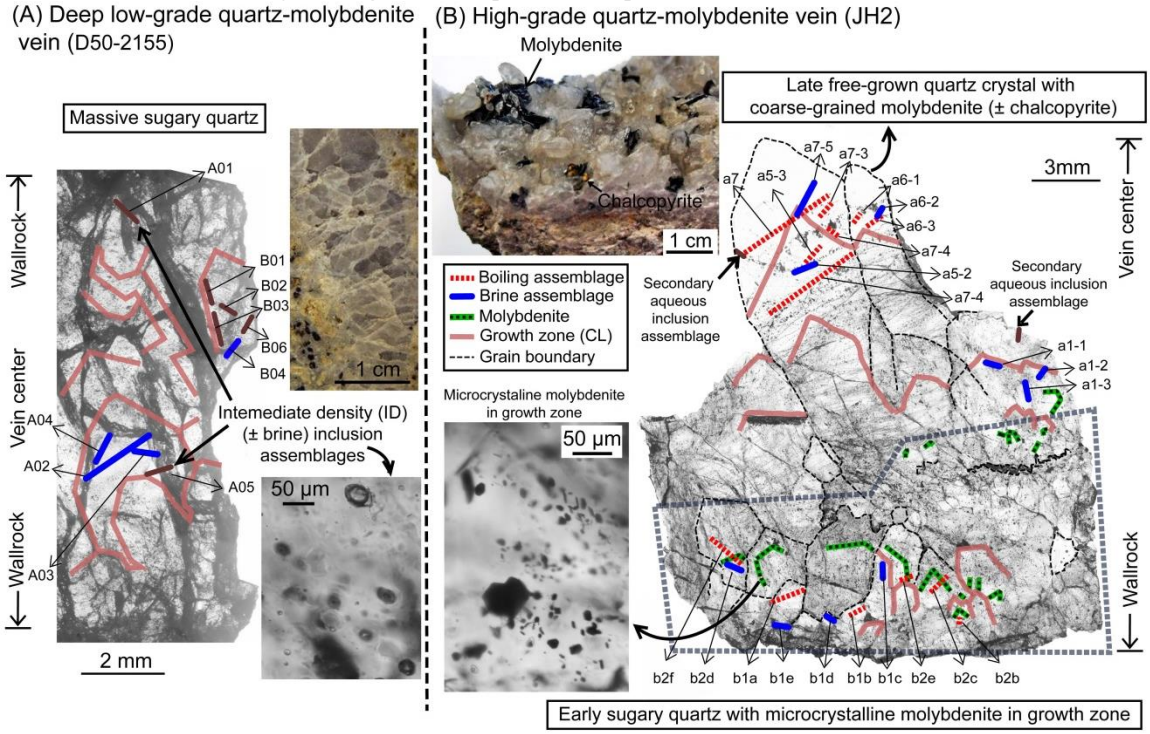

Figure 3. Quartz vein textures and locations of fluid inclusion assemblages in the low-grade (A; D50-2155) and high-grade (B; JH2) quartz-molybdenite veins. Growth zones in quartz were determined from a cathodo-luminescence image taken by SEM, and by optical microscopy. (A) Massive sugary quartz crystal grown in the deep low-grade quartz-molybdenite vein contains intermediate-density fluid inclusions. Some intermediate-density fluid inclusions are associated with brine inclusions. (B) Two stages of quartz textures were observed in the high grade quartz-molybdenite vein. Early sugary quartz crystals grown along the wallrock have microcrystalline molybdenite in growth-zone, which is texturally similar to the low grade quartz-molybdenite vein (A). The early massive sugary quartz crystals were overgrown by texturally-late euhedral free-standing quartz crystals. This free-standing quartz crystals are closely associated with precipitations of coarse-grained molybdenite and local precipitation of euhedral chalcopyrite in the vein center, see the sample figure at (B). Numerous pseudo-secondary or secondary brines, vapors, and boiling assemblages are associated with early sugary quartz crystals and late free-standing quartz crystals.

Low and high-grade quartz-molybdenite veins were sampled where we had clear evidence that they cut late QLP dikes and their contacts with earlier lithologies (EM, QMP, and LP). Low-grade quartz-molybdenite veins (Low-grade Mo-stage; D50-2155, 2379) were sampled in the deep barren core of the mine (elevations of 1,000-1,100 m above sea level). They were selected because they showed the same crosscutting relationship and contain a minor

amount of molybdenite, as tiny dispersed crystals (D50-2155) or as a fine selvage of molybdenite grown from the wallrock (D50-2379). These weakly Mo-mineralized veins are interpreted to be low-grade versions of the main-stage (high-grade) quartz-molybdenite veins located higher up in the deposit. They contain CO_2-bearing intermediate-density inclusions (Fig. 3A) and some brine inclusions. High-grade quartz-molybdenite veins (High-grade Mo-stage; JH2, JH4, D511-3120, A51-4640, 4990-1470, A57-5931, A57-6093 and D511-3120) were collected from the open pit surface at 2007 and from drill cores of the deep periphery in the mine (Fig. 1). High-grade quartz-molybdenite veins sampled from the high-grade center (elevations of 1,400-1,500 m above sea level; JH2, JH4, and 4990-1470) and contain mainly brine and vapor inclusions, whereas samples from the deep periphery (elevations of 300-800 m above sea level; A51-4640, A57-5931, A57-6093 and D511-3120) contain intermediate-density fluid inclusions.

In high-grade quartz-molybdenite veins, molybdenite precipitated throughout the paragenetic sequence. Early microcrystalline or massive flaky molybdenite commonly overgrew the contact with the wallrock and predated sugary quartz (Fig. 3B). Fine-grained sugary quartz was overgrown by euhedral quartz crystals. Coarse flakes of molybdenite were deposited at the base of the large euhedral quartz crystals overgrowing sugary quartz (Fig. 3B) or as hexagonal platelets on top of the quartz crystals in the vein center (Fig. 2A). In the central vug of many quartz-molybdenite veins, euhedral chalcopyrite and finally calcite have overgrown quartz and molybdenite (Fig. 2C). Quartz veins of all generations contain vapor, brine, and commonly coexisting vapor and brine inclusions. The quartz molybdenite veins are hosted in potassic alteration of QLP, but commonly show a weak halo of overprinting muscovite or clay alteration (Table 1).

Textures were studied by optical microscopy and cathodoluminescence images taken by scanning electron microscopy (Fig. 3, 4). Low-grade quartz-molybdenite veins located at the deep barren core have massive quartz without open vugs (Fig. 4A). A cathodoluminescence image of this sugary quartz reveals microscopic euhedral growth perpendicularly away from the wall rock (Fig. 4A). Similar texture can be observed in the basal zone of a high-grade quartz-molybdenite vein (sugary quartz; Fig. 3B, 4B, 4C), intergrown with microcrystalline molybdenite along growth zones of quartz. The sugary quartz zone is overgrown by texturally similar, but coarser-grained euhedral free-standing quartz crystals and large flakes of molybdenite (Fig. 3B and Fig. 4B). These textures confirm that the two quartz generations (sugary and free-standing quartz) overlapped with molybdenite deposition temporally. Cathodoluminescence images of some of the quartz-molybdenite veins show evidence of minor redissolution and reprecipitation of a second generation of quartz (Fig. 4), similar to the Cu-stage quartz stockwork veins (Redmond et al., 2004; Landtwing et al., 2005; Landtwing et al., 2010).

Methods

Representative fluid inclusion assemblages (FIA) were selected by detailed petrography and checked by microthermometry to confirm that they show consistent microthermetric behavior, such as halite dissolution and homogenization temperatures. Obtaining microthermometric properties of CO_2-bearing vapor inclusions was, in most cases, difficult because of thin film of aqueous liquid lining the walls of the inclusions and the formation of clathrates. Homogenization temperatures of vapor inclusions were assumed to be equivalent to those of coexisting brine inclusions in sets of texturally-proven cogenetic brine and vapor "boiling" assemblage. Homogenization temperatures of the brine inclusions in the boiling assemblages were combined with the apparent brine salinities (wt% NaCl eq.) to estimate the fluid pressure of the entrapment condition, based on the two-phase surface NaCl-H_2O model system (Driesner and Heinrich, 2007).

Table 1. Descriptions of the quartz vein samples from drill core and mine outcrops that were used for fluid inclusion analyses.

sample #	host rock	location, elevation above sea level	mineralogy, quartz texture, alteration
Deep, quartz stockwork vein at barren core (low-grade Cu-stage)			
A35-4561	QMP	Central, 650 m	8 mm blocky fine grain quartz vein, chalcopyrite ± pyrite. Biotite alteration
A30-3816	QMP	Central, 750 m	1 cm blocky quartz vein with chalcopyrite ± pyrite. Biotite alteration
A30-3836	QMP	Central, 750 m	1 cm blocky quartz vein with chalcopyrite ± pyrite. Biotite alteration
Quartz stockwork vein at high-grade center (high-grade Cu-stage)			
D211-19	QMP	Central, 1600 m	Gray-clear blocky (sometimes vuggy) quartz vein with chalcopyrite (chalcopyrite occur at the interstitials of early generation of quartz; Landtwing et al., 2005). Biotite alteration.
Deep, quartz-molybdenite vein at barren core (low-grade Mo-stage)			
D50-2155	QLP	Central, 1090 m	1 cm fine to coarse grain blocky quartz vein ± molybdenite. Weak muscovite alteration.
D50-2379	QLP	Central, 1024 m	1 cm coarse grain blocky quartz vein with molybdenite ± pyrite (molybdenite grown from the wallrock). Biotite & muscovite alteration.
Quartz-molybdenite vein at high-grade center and deep periphery (high-grade Mo-stage)			
4990-1470 (2-types of veins)	QLP	Central, 1500 m	QMP clast entrained in QLP host. Two generations of quartz veins. 1) Post-QLP late stockwork vein with gray-clear quartz (digenite) vein with bornite alterations crosscut by 2) buggy and clear quartz-molybdenite vein (molybdenite grown from the wallrock and late euhedral chalcopyrite occured at vein center). Weak muscovite alteration around the quartz-molybdenite vein.
JH2	QLP	Central, 1430 m	Two generatons of molybdenite deposition at the single vein; 1) microcrystaline molybdenite within growthzone of early sugary (blocky) quartz overgrown by 2) euhedral, freestanding quartz vein with coarser molybdenite ± late euhedral chalcopyrite. The vein cuts early stockwork veinlets. Muscovite alteration around quartz-molybdenite vein.

JH4	EM&QLP	Central, 1460 m	Thick quartz vein with freestanding quartz crystals with flakes of molybdenite interstitially growned ± late euhedral chalcopyrite. The vein cuts also EM. Muscovite alteration.
D511-3120	QLP	Peripheral, 830 m	8 mm coarse grain blocky quartz vein with molybdenite (molybdenite grown at centerline). Vug filled calcite. Muscovite alteration. The vein cuts early biotite-altered quartz veinlets.
A51-4640	QMP&QLP	Peripheral, 640 m	Contact of QLP and QMP. 8 mm of clear (buggy sometimes) quartz-molybdenite veinlet (molybdenite grown at centerline) cutting QMP hosted stockwork veinlets and QLP. Weak muscovite alteration.
A57-5931	QMP&QLP	Peripheral, 330 m	8 mm fine sugary quartz vein with molybdenite (molybdenite grown at centerline). The vein cuts contact of QMP and QLP. Biotite alteration
A57-6093	QMP&QLP	Peripheral, 350 m	Two generations of quartz veins; 1) 6 mm milky quartz vein, 2) 1 mm two fine-grained quartz moybdenite veins ± pyrite. These cut the earlier milky quartz vein. Biotite alteration.

EM = equigranular monzonite, QMP = quartz monzonite porphyry, QLP = quartz latite porphyry.

Table 2. Composition of Cu-stage (quartz stockwork veins) brine inclusion assemblages in the Bingham Canyon deposit.

μg/g	Location	Sample#	Sal.	Th(℃)	P(bar)	^{23}Na	^{32}S	^{39}K	^{57}Fe	^{65}Cu	^{75}As	^{133}Cs	^{197}Au	^{208}Pb	^{66}Zn	^{95}Mo	mark
Av.	**center**	**A30-3816**	**41.9**	**332**	**ND**	**120 000**	**8 400**	**96 000**	**50 000**	**10 000**	**46**	**49**	**0.26**	**3 300**	**3 400**	**6.6**	**boil**
SD	Deep stw.	4_TP7	0.6	13		3 100	4 700	7 800	4 300	1 000	7	9	0.12	290	370	4.0	
Av.	**center**	**A30-3816**	**40.4**	**389**	**173**	**120 000**	**4 800**	**100 000**	**39 000**	**7 800**	**30**	**48**	**0.42**	**3 300**	**2 700**	**170**	**boil**
SD	Deep stw.	4_TP8	0.8	6	realPT	2 100	1 600	5 400	3 100	2 500	5	6	0.13	160	340	100	
Av.	**center**	**A30-3816**	**39.0**	**380**	**162**	**110 000**	**6 400**	**100 000**	**50 000**	**6 000**	**40**	**49**	**0.24**	**2 900**	**3 800**	**12**	**boil**
SD	Deep stw.	4_TP9(b)	0.6	25	realPT	1 300	2 200	3 400	13 000	6 400	15	12	0.12	140	1 400	15	
Av.	**center**	**A30-3816**	**36.5**	**374**	**155**	**100 000**	**6 100**	**100 000**	**40 000**	**7 700**	**37**	**42**	**0.21**	**3 500**	**3 300**	**51**	**boil**
SD	Deep stw.	4_TP10(b)	0.6	16	realPT	6 200	2 900	15 000	8 800	2 900	12	19	0.23	590	1 600	71	
Av.	**center**	**A30-3816**	**36.1**	**381**	**168**	**97 000**	**12 000**	**110 000**	**50 000**	**10 000**	**38**	**53**	**0.22**	**3 100**	**4 100**	**50**	**boil**
SD	Deep stw.	4_TP11(b)	0.4	15	realPT	1 300	4 200	4 100	4 400	1 400	3	6	0.09	330	550	31	
Av.	**center**	**A35-4561**	**34.4**	**323**	**88**	**97 000**	**7 600**	**52 000**	**36 000**	**7 600**	**57**	**64**	**0.14**	**2 800**	**ND**	**440**	**boil**
SD	Deep stw.	1-TP2(b)	1.8	15	realPT	17 000	4 500	42 000	11 000	6 100	37	47	0.06	1 700	ND	470	
Av.	**center**	**A35-4561**	**36.8**	**379**	**162**	**120 000**	**5 200**	**61 000**	**31 000**	**5 700**	**33**	**39**	**0.43**	**2 300**	**2 300**	**380**	**boil**
SD	Deep stw.	1_TP3	1.4	13	realPT	2 100	1 700	5 600	2 100	210	7	6	0.09	76	180	24	
Av.	**center**	**A35-4561**	**30.0**	**379**	**176**	**100 000**	**8 200**	**47 000**	**36 000**	**7 600**	**59**	**33**	**ND**	**2 100**	**3 000**	**59**	**boil**
SD	Deep stw.	1_TP4	0.6	14	realPT	2 500	4 400	6 100	3 800	1 200	34	17	ND	100	760	19	
Av.	**center**	**A35-4561**	**34.3**	**363**	**142**	**110 000**	**7 400**	**57 000**	**33 000**	**7 900**	**25**	**23**	**ND**	**2 400**	**2 800**	**330**	**boil**
SD	Deep stw.	1_TP5	1.5	26	realPT	5 800	280	14 000	9 100	4 000	ND	17	ND	450	1 000	20	
Av.	**center**	**A35-4561**	**36.0**	**363**	**138**	**110 000**	**3 600**	**65 000**	**45 000**	**3 900**	**38**	**45**	**1.10**	**2 700**	**2 800**	**220**	**boil**
SD	Deep stw.	1_TP6	0.9	8	realPT	990	1 800	2 300	17 000	1 500	6	4	0.80	340	670	160	
Av.	**center**	**A30-3836**	**39.2**	**313**	**ND**	**110 000**	**3 700**	**100 000**	**49 000**	**7 500**	**49**	**52**	**0.80**	**3 100**	**2 400**	**330**	**no-boil**
SD	Deep stw.	1_B1	0.0	15		7 700	1 300	19 000	11 000	1 400	10	13	ND	550	660	160	
Av.	**center**	**A30-3836**	**38.7**	**371**	**146**	**110 000**	**4 300**	**100 000**	**49 000**	**7 400**	**37**	**49**	**0.49**	**3 200**	**2 700**	**340**	**no-boil**
SD	Deep stw.	1_B2	0.4	18	minPT	3 400	1 600	8 600	3 000	3 800	5	6	0.27	530	750	95	
Av.	**center**	**A30-3836**	**37.9**	**328**	**89**	**110 000**	**10 000**	**82 000**	**39 000**	**9 500**	**13**	**43**	**1.80**	**2 800**	**2 100**	**180**	**no-boil**
SD	Deep stw.	1_B3	0.9	3	minPT	4 500	7 700	11 000	2 700	2 000	ND	8	ND	63	250	110	
Av.	**center**	**A30-3836**	**40.1**	**326**	**ND**	**120 000**	**3 600**	**98 000**	**41 000**	**7 200**	**33**	**44**	**0.69**	**2 900**	**3 500**	**120**	**no-boil**
SD	Deep stw.	1_TP1	0.2	14		9 000	2 200	21 000	7 800	2 800	16	18	ND	880	1 900	20	
Av.	**center**	**D211-19**	**50.9**	**369**	**ND**	**150 000**	**2 500**	**120 000**	**56 000**	**450**	**110**	**53**	**2.00**	**5 000**	**4 500**	**6.6**	**no-boil**
SD	Cu-vein	1_B1	2.8	26		4 500	550	11 000	12 000	170	37	7	ND	840	940	7.6	

Av.	**center**	**D211-19**	**47.8**	**385**	**ND**	**130 000**	**11 000**	**120 000**	**72 000**	**1 100**	**35**	**42**	**ND**	**4 800**	**4 300**	**42.0**	**boil**
SD	Cu-vein	1_B2	0.8	14		7 500	3 000	18 000	4 600	280	22	6	ND	1 100	1 000	5.7	
Av.	**center**	**D211-19**	**52.9**	**400**	**ND**	**140 000**	**5 600**	**150 000**	**94 000**	**2 800**	**44**	**60**	**0.31**	**5 900**	**5 900**	**47.0**	**boil**
SD	Cu-vein	1_B3	2.0	16		13 000	3 000	30 000	29 000	2 600	19	17	0.17	2 300	3 100	38.0	
Av.	**center**	**D211-19**	**52.2**	**392**	**ND**	**150 000**	**5 000**	**120 000**	**96 000**	**2 800**	**38**	**52**	**1.00**	**5 700**	**5 500**	**100.0**	**boil**
SD	Cu-vein	1_B4	1.3	8		2 600	1 900	3 400	11 000	670	13	11	0.64	1 300	1 500	110.0	
Av.	**center**	**D211-19**	**51.8**	**373**	**ND**	**140 000**	**2 600**	**140 000**	**140 000**	**870**	**61**	**110**	**0.34**	**6 700**	**7 000**	**6.7**	**boil**
SD	Cu-vein	1_B5	0.1	23		9 200	1 400	22 000	40 000	300	14	39	ND	1 800	1 800	7.9	
Av.	**center**	**D211-19**	**49.6**	**378**	**ND**	**140 000**	**7 100**	**130 000**	**62 000**	**1 300**	**70**	**42**	**ND**	**4 100**	**3 800**	**19.0**	**boil**
SD	Cu-vein	1_B6	ND	ND		8 700	3 500	22 000	25 000	760	45	18	ND	1 000	980	17.0	
Av.	**center**	**D211-19**	**43.3**	**393**	**174**	**120 000**	**5 400**	**110 000**	**61 000**	**5 700**	**54**	**36**	**ND**	**4 100**	**3 600**	**29.0**	**no-boil**
SD	Cu-vein	1_B7	4.6	22	minPT	4 800	3 500	10 000	33 000	3 700	40	1	ND	1 500	1 200	ND	
Av.	**center**	**D211-19**	**43.3**	**393**	**174**	**110 000**	**15 000**	**130 000**	**100 000**	**18 000**	**71**	**40**	**ND**	**5 900**	**5 500**	**160.0**	**no-boil**
SD	Cu-vein	1_B7-1	4.6	22	minPT	9 400	5 000	25 000	5 200	12 000	26	9	ND	860	540	180.0	
Av.	**center**	**D211-19**	**39.7**	**430**	**261**	**110 000**	**7 200**	**98 000**	**65 000**	**1 000**	**35**	**34**	**ND**	**3 500**	**3 000**	**56.0**	**boil**
SD	Cu-vein	1_B8	1.1	7	realPT	1 900	430	4 700	2 000	200	7	8	ND	360	180	66.0	
Av.	**center**	**D211-19**	**43.1**	**417**	**221**	**120 000**	**5 500**	**110 000**	**64 000**	**920**	**47**	**47**	**0.30**	**3 800**	**2 700**	**100.0**	**no-boil**
SD	Cu-vein	1_B9	0.2	9	minPT	3 800	1 300	8 600	6 800	150	15	2	0.26	880	1 100	43.0	
Av.	**center**	**D211-19**	**46.2**	**410**	**196**	**140 000**	**4 900**	**100 000**	**45 000**	**2 500**	**71**	**47**	**0.10**	**3 300**	**2 900**	**360.0**	**boil**
SD	Cu-vein	1_B10	0.8	28	realPT	ND	ND	ND	ND	ND	ND	ND	ND	ND	ND	ND	
Av.	**center**	**4990-1470**	**43.7**	**391**	**170**	**120 000**	**2 900**	**110 000**	**47 000**	**560**	**56**	**39**	**0.76**	**3 500**	**3 000**	**83**	**no-boil**
SD	QLP stw.	1_B1	0.8	3	minPT	1 000	1 500	2 000	1 200	14	1.4	3	0.65	220	460	2	
Av.	**center**	**4990-1470**	**39.7**	**364**	**134**	**110 000**	**4 800**	**93 000**	**51 000**	**1 000**	**34**	**46**	**0.23**	**2 700**	**2 300**	**72**	**no-boil**
SD	QLP stw.	1_B2	0.6	14	minPT	11 000	2 600	26 000	10 000	450	12	17	ND	520	640	70	

Averages (Av.; µg/g) and standard deviations (SD; 1 sigma) of elements in Cu-stage (quartz stockwork veins). Salinities (Sal.; equivalent NaCl wt %) and homogenization temperatures (T_h) of the assemblages were obtained from microthermometry (Bodnar and Vityk, 1994) and pressures of entrapment were estimated (Driesner and Heinrich, 2007). "Deep stw.", "Cu-vein", and "QLP stw" represent low Cu grade quartz stockwork veins, high Cu grade quartz stockwork vein, and late-stage (post-QLP) quartz stockwork vein, respectively. Boiling assemblages "boil" allow direct calculation "real PT" of pressures, whereas brine-only "no-boil" assemblages provide minimum estimation "min PT" of pressures. "ND" represents values not determined.

Table 3. Composition of Mo-stage (quartz-molybdenite veins) brine inclusion assemblages

μg/g	Location	Sample#	Sal.	Th(℃)	P(bar)	^{23}Na	^{32}S	^{39}K	^{57}Fe	^{65}Cu	^{75}As	^{133}Cs	^{197}Au	^{208}Pb	^{66}Zn	^{95}Mo	mark
Av.	**center**	**D50-2155**	**41.4**	**469**	**362**	**110 000**	**5 600**	**110 000**	**48 000**	**300**	**39**	**54**	**0.16**	**3 100**	**2 800**	**160.0**	**boil**
SD	deep Moly	A02	0.4	22	realPT	5 900	1 200	15 000	6 100	74	5	9	0.07	490	520	100.0	
Av.	**center**	**D50-2155**	**42.0**	**426**	**245**	**120 000**	**6 100**	**100 000**	**41 000**	**360**	**29**	**46**	**0.41**	**3 200**	**2 500**	**380.0**	**no-boil**
SD	deep Moly	A03	1.0	21	minPT	2 800	1 300	7 300	4 700	100	10	5	0.10	350	290	8.6	
Av.	**center**	**D50-2155**	**40.0**	**426**	**251**	**110 000**	**5 700**	**99 000**	**49 000**	**250**	**30**	**48**	**0.26**	**3 000**	**2 700**	**75.0**	**no-boil**
SD	deep Moly	A04	0.5	15	minPT	710	500	1 800	1 900	47	5	6	ND	59	91	5.9	
Av.	**center**	**D50-2155**	**42.0**	**498**	**447**	**120 000**	**3 700**	**100 000**	**44 000**	**750**	**35**	**46**	**0.21**	**2 900**	**2 400**	**130.0**	**boil**
SD	deep Moly	A05	0.8	8	realPT	1 300	2 300	3 300	2 300	740	11	5	0.17	210	360	110.0	
Av.	**center**	**D50-2155**	**40.2**	**404**	**205**	**120 000**	**7 200**	**97 000**	**39 000**	**920**	**35**	**39**	**0.11**	**2 600**	**2 300**	**87.0**	**boil**
SD	deep Moly	B01	1.7	28	realPT	1 400	510	3 400	4 300	600	4	3	0.03	340	390	14.0	
Av.	**center**	**D50-2155**	**41.5**	**412**	**217**	**130 000**	**7 100**	**81 000**	**35 000**	**720**	**27**	**38**	**0.55**	**2 600**	**1 900**	**77.0**	**boil**
SD	deep Moly	B02	0.9	17	realPT	9 200	1 800	24 000	18 000	890	10	8	0.41	450	760	37.0	
Av.	**center**	**D50-2155**	**36.9**	**416**	**240**	**110 000**	**7 100**	**88 000**	**39 000**	**1 200**	**28**	**37**	**0.30**	**2 600**	**2 400**	**97.0**	**boil**
SD	deep Moly	B03	0.9	21	realPT	2 400	2 800	6 800	5 900	1 600	3	3	0.03	360	290	33.0	
Av.	**center**	**D50-2155**	**42.3**	**403**	**197**	**130 000**	**3 200**	**97 000**	**39 000**	**1 500**	**24**	**29**	**0.26**	**2 800**	**1 800**	**150.0**	**boil**
SD	deep Moly	B04	1.4	33	realPT	6 200	1 900	15 000	18 000	980	10	12	0.26	380	970	120.0	
Av.	**center**	**D50-2155**	**40.7**	**399**	**193**	**110 000**	**7 900**	**110 000**	**51 000**	**340**	**30**	**55**	**0.22**	**3 000**	**3 200**	**100.0**	**boil**
SD	deep Moly	B06	0.7	40	realPT	3 200	2 800	7 300	14 000	140	9	19	0.00	350	1 000	64.0	
Av.	**center**	**D50-2379**	**41.1**	**295**	**ND**	**14 000**	**7 600**	**68 000**	**33 000**	**7 900**	**74**	**32**	**1.90**	**2 500**	**2 500**	**360.0**	**boil**
SD	deep Moly	1_B3	1.5	6		1 200	2 100	4 900	1 900	1 900	59	8	0.10	240	870	420.0	
Av.	**center**	**D50-2379**	**40.5**	**273**	**ND**	**130 000**	**7 100**	**64 000**	**11 000**	**1 200**	**240**	**47**	**ND**	**6 200**	**5 800**	**ND**	**boil**
SD	deep Moly	1_TP1	2.1	33		3 900	4 400	10 000	3 900	740	23	9	ND	1 800	1 000	ND	
Av.	**center**	**D50-2379**	**50.6**	**275**	**ND**	**170 000**	**4 700**	**71 000**	**44 000**	**4 600**	**64**	**51**	**1.70**	**3 300**	**3 400**	**ND**	**boil**
SD	deep Moly	1_B5	0.8	7		5 900	240	15 000	5 300	2 300	8	5	ND	370	280	ND	
Av.	**center**	**D50-2379**	**44.0**	**289**	**ND**	**140 000**	**5 700**	**76 000**	**43 000**	**5 700**	**48**	**44**	**0.81**	**3 300**	**3 200**	**150.0**	**boil**
SD	deep Moly	1_TP4	0.3	12		9 500	2 800	24 000	7 800	3 900	18	15	0.60	850	1 000	190.0	
Av.	**center**	**JH2**	**45.2**	**475**	**357**	**120 000**	**9 200**	**73 000**	**53 000**	**3 600**	**55**	**43**	**2.30**	**3 300**	**4 000**	**47.0**	**no-boil**
SD	Mo-vein	b1e	1.0	ND	minPT	9 000	2 500	13 000	8 200	1 400	37	10	2.30	240	1 400	20.0	
Av.	**center**	**JH2**	**40.9**	**413**	**220**	**99 000**	**21 000**	**98 000**	**53 000**	**16 000**	**25**	**39**	**0.68**	**3 400**	**3 000**	**380.0**	**boil**
SD	Mo-vein	b1b	1.8	12	realPT	18 000	4 700	36 000	17 000	6 300	10	19	0.30	1 100	1 100	170.0	
Av.	**center**	**JH2**	**47.7**	**414**	**200**	**120 000**	**14 000**	**90 000**	**62 000**	**10 000**	**30**	**57**	**0.26**	**3 500**	**3 800**	**120.0**	**boil**
SD	Mo-vein	b1a	1.1	11	realPT	4 700	4 400	13 000	5 900	4 000	6	5	0.02	340	840	47.0	

Av.	**center**	**JH2**	**45.4**	**399**	**179**	**100 000**	**25 000**	**100 000**	**65 000**	**24 000**	**12**	**39**	**4.60**	**4 400**	**4 500**	**360.0**	**no-boil**
SD	Mo-vein	b1d	1.7	12	minPT	22 000	11 000	53 000	14 000	4 200	0	15	6.40	2 800	3 300	220.0	
Av.	**center**	**JH2**	**41.3**	**572**	**691**	**110 000**	**2 900**	**86 000**	**42 000**	**910**	**34**	**39**	**0.25**	**2 400**	**1 800**	**38.0**	**no-boil**
SD	Mo-vein	b1c	1.0	11	minPT	6 100	1 100	12 000	4 300	150	8	7	0.12	230	380	18.0	
Av.	**center**	**JH2**	**46.4**	**415**	**207**	**120 000**	**12 000**	**83 000**	**52 000**	**5 700**	**56**	**46**	**0.71**	**3 500**	**5 000**	**93.0**	**boil**
SD	Mo-vein	b2b	3.9	21	realPT	13 000	8 200	19 000	18 000	4 700	23	14	0.29	930	1 800	110.0	
Av.	**center**	**JH2**	**43.4**	**469**	**351**	**100 000**	**11 000**	**100 000**	**55 000**	**16 000**	**20**	**33**	**0.31**	**2 800**	**2 300**	**350.0**	**boil**
SD	Mo-vein	b2c	0.3	4	realPT	3 800	1 900	8 600	4 100	1 700	7	7	0.11	660	350	84.0	
Av.	**center**	**JH2**	**42.1**	**428**	**249**	**100 000**	**11 000**	**85 000**	**58 000**	**13 000**	**28**	**27**	**1.50**	**2 800**	**2 900**	**360.0**	**boil**
SD	Mo-vein	b2e	0.4	11	realPT	8 900	1 700	13 000	8 400	1 900	13	7	2.00	250	760	59.0	
Av.	**center**	**JH2**	**47.7**	**407**	**187**	**120 000**	**6 800**	**100 000**	**51 000**	**1 000**	**23**	**44**	**0.19**	**3 200**	**3 000**	**72.0**	**no-boil**
SD	Mo-vein	b2d	0.2	2	minPT	4 600	1 200	8 000	5 100	630	6	10	0.11	170	520	8.7	
Av.	**center**	**JH2**	**39.3**	**542**	**609**	**100 000**	**8 300**	**89 000**	**36 000**	**530**	**22**	**25**	**0.42**	**2 100**	**1 700**	**25.0**	**boil**
SD	Mo-vein	b2f	0.3	30	realPT	9 800	3 700	9 700	15 000	270	11	12	0.49	570	830	7.2	
Av.	**center**	**JH2**	**39.3**	**325**	**84**	**100 000**	**7 400**	**69 000**	**41 000**	**6 900**	**18**	**29**	**1.20**	**2 600**	**2 000**	**83.0**	**no-boil**
SD	Mo-vein	a1-1	2.7	ND	minPT	6 300	1 800	10 000	8 100	4 600	3	12	0.24	430	670	46.0	
Av.	**center**	**JH2**	**42.0**	**ND**	**ND**	**110 000**	**3 600**	**83 000**	**41 000**	**390**	**45**	**33**	**0.29**	**2 600**	**2 100**	**5.4**	**no-boil**
SD	Mo-vein	a1-2	1.8	ND		10 000	510	15 000	11 000	260	21	10	0.17	540	680	1.3	
Av.	**center**	**JH2**	**39.3**	**330**	**89**	**100 000**	**6 800**	**82 000**	**44 000**	**310**	**25**	**42**	**0.37**	**2 800**	**2 700**	**33.0**	**no-boil**
SD	Mo-vein	a1-3	0.8	8	minPT	9 200	2 600	16 000	6 200	190	3	12	ND	680	900	13.0	
Av.	**center**	**JH2**	**44.4**	**475**	**362**	**110 000**	**8 500**	**100 000**	**53 000**	**780**	**27**	**48**	**0.31**	**2 900**	**2 800**	**140.0**	**no-boil**
SD	Mo-vein	a5-2	0.7	7	minPT	6 200	1 900	15 000	3 600	150	3	4	0.22	780	360	21.0	
Av.	**center**	**JH2**	**42.1**	**580**	**709**	**110 000**	**6 800**	**96 000**	**40 000**	**200**	**33**	**36**	**0.40**	**2 700**	**2 800**	**1.8**	**boil**
SD	Mo-vein	a5-3	0.1	30	realPT	2 600	2 200	3 600	4 200	34	2	5	0.17	400	440	1.0	
Av.	**center**	**JH2**	**46.2**	**411**	**200**	**110 000**	**23 000**	**100 000**	**58 000**	**25 000**	**24**	**47**	**0.16**	**3 100**	**3 200**	**88.0**	**boil**
SD	Mo-vein	a6-1	1.0	4	realPT	1 600	2 300	8 700	6 100	2 500	7	3	ND	260	460	50.0	
Av.	**center**	**JH2**	**49.3**	**431**	**227**	**110 000**	**23 000**	**120 000**	**62 000**	**27 000**	**16**	**47**	**0.64**	**3 300**	**3 200**	**26.0**	**no-boil**
SD	Mo-vein	a6-2	0.5	ND	minPT	4 800	4 700	7 200	4 700	3 000	3	6	0.49	380	450	5.9	
Av.	**center**	**JH2**	**46.8**	**425**	**225**	**110 000**	**11 000**	**110 000**	**57 000**	**520**	**22**	**42**	**0.25**	**3 100**	**3 200**	**110.0**	**boil**
SD	Mo-vein	a6-3	1.5	3	realPT	2 800	3 700	6 300	3 600	190	10	6	0.12	530	750	13.0	
Av.	**center**	**JH2**	**49.9**	**429**	**221**	**130 000**	**17 000**	**110 000**	**52 000**	**16 000**	**13**	**43**	**0.29**	**2 900**	**2 900**	**20.0**	**boil**
SD	Mo-vein	a7	0.4	ND	realPT	7 400	3 100	15 000	6 700	9 500	4	4	0.12	220	1 000	20.0	
Av.	**center**	**JH2**	**45.8**	**431**	**242**	**100 000**	**24 000**	**120 000**	**59 000**	**2 700**	**26**	**60**	**0.45**	**4 000**	**4 100**	**110.0**	**boil**
SD	Mo-vein	a7-1	1.4	3	realPT	11 000	9 700	21 000	7 400	3 300	8	13	0.26	870	1 200	45.0	
Av.	**center**	**JH2**	**43.4**	**427**	**243**	**88 000**	**5 300**	**85 000**	**33 000**	**220**	**23**	**39**	**0.14**	**2 400**	**2 400**	**130.0**	**boil**

SD	Mo-vein	a7-3	0.8	16	realPT	7 500	2 000	9 500	8 600	150	4	10	0.07	370	550	41.0	
Av.	**center**	**JH2**	**39.0**	**580**	**742**	**97 000**	**5 100**	**85 000**	**52 000**	**190**	**27**	**37**	**0.20**	**2 800**	**2 300**	**51.0**	**no-boil**
SD	Mo-vein	a7-4	0.5	minT	minPT	4 700	1 600	3 000	8 600	62	6	8	0.02	310	450	10.0	
Av.	**center**	**JH2**	**59.4**	**ND**	**ND**	**160 000**	**6 600**	**110 000**	**50 000**	**580**	**30**	**61**	**0.09**	**4 000**	**3 400**	**18.0**	**no-boil**
SD	Mo-vein	a7-5	2.0	ND		6 000	1 300	10 000	5 700	78	4	11	0.05	380	320	1.5	
Av.	**center**	**JH2**	**39.7**	**526**	**553**	**100 000**	**4 500**	**83 000**	**45 000**	**540**	**29**	**42**	**0.07**	**2 500**	**2 400**	**7.2**	**boil**
SD	Mo-vein	a7-6	ND	11	realPT	5 400	940	8 000	5 200	190	4	4	0.03	430	630	3.2	
Av.	**center**	**JH2**	**41.2**	**492**	**434**	**120 000**	**6 000**	**79 000**	**39 000**	**1 200**	**51**	**42**	**1.30**	**3 800**	**ND**	**88.0**	**boil**
SD	Mo-vein	B_BT2	2.1		realPT	10 000	3 200	11 000	13 000	950	31	7	1.00	970	ND	80.0	
Av.	**periphery**	**D511-3120**	**40.2**	**ND**	**ND**	**120 000**	**13 000**	**95 000**	**60 000**	**8 800**	**59**	**38**	**ND**	**2 900**	**3 600**	**30.0**	**no-boil**
SD	Mo-vein	1_B2	0.6	ND		1 500	2 600	3 900	4 600	8 200	19	9	ND	190	310	4.9	
Av.	**periphery**	**D511-3120**	**37.5**	**381**	**166**	**110 000**	**8 800**	**82 000**	**38 000**	**8 100**	**24**	**35**	**ND**	**2 700**	**2 600**	**31.0**	**no-boil**
SD	Mo-vein	1_B3	0.5	5	minPT	3 300	4 200	9 600	1 600	6 000	12	10	ND	490	340	30.0	
Av.	**periphery**	**D511-3120**	**35.3**	**360**	**136**	**100 000**	**12 000**	**90 000**	**40 000**	**9 100**	**35**	**32**	**3.60**	**2 500**	**2 900**	**76.0**	**boil**
SD	Mo-vein	1_TP4	1.3	17	realPT	3 500	4 500	9 200	1 600	1 100	22	7	0.24	140	380	27.0	
Av.	**periphery**	**D511-3120**	**42.0**	**319**	**ND**	**120 000**	**17 000**	**94 000**	**46 000**	**11 000**	**82**	**51**	**1.60**	**2 700**	**2 900**	**130.0**	**no-boil**
SD	Mo-vein	1_B5	0.1	13		86	11 000	340	7 500	860	66	18	ND	250	67	42.0	
Av.	**periphery**	**D511-3120**	**37.1**	**377**	**160**	**110 000**	**10 000**	**80 000**	**43 000**	**10 000**	**36**	**36**	**ND**	**2 500**	**2 800**	**120.0**	**boil**
SD	Mo-vein	1_TP6(b)	0.9	20	realPT	4 200	1 200	10 000	5 000	3 200	6	8	ND	110	730	65.0	
Av.	**periphery**	**D511-3120**	**37.1**	**ND**	**ND**	**110 000**	**16 000**	**90 000**	**56 000**	**10 000**	**28**	**63**	**13.00**	**2 500**	**5 400**	**76.0**	**no-boil**
SD	Mo-vein	1_B7	ND	ND		13 000	4 500	30 000	22 000	2 600	ND	43	ND	460	4 100	18.0	
Av.	**center**	**JH4**	**39.4**	**ND**	**ND**	**87 000**	**7 100**	**55 000**	**29 000**	**1 200**	**ND**	**ND**	**ND**	**1 900**	**ND**	**1.7**	**no-boil**
SD	Mo-vein	a_B1	ND	ND		5 700	4 900	4 800	2 300	470	ND	ND	ND	410	ND	ND	
Av.	**center**	**JH4**	**47.2**	**ND**	**ND**	**100 000**	**4 300**	**68 000**	**37 000**	**830**	**ND**	**ND**	**ND**	**2 100**	**ND**	**6.5**	**no-boil**
SD	Mo-vein	a_B2	ND	ND		6 600	3 400	10 000	2 200	480	ND	ND	ND	270	ND	3.2	
Av.	**center**	**JH4**	**39.1**	**ND**	**ND**	**81 000**	**3 000**	**58 000**	**33 000**	**590**	**ND**	**ND**	**ND**	**1 800**	**ND**	**1.9**	**no-boil**
SD	Mo-vein	a_B3	1.3	ND		2 900	2 300	2 000	1 200	390	ND	ND	ND	140	ND	0.3	
Av.	**center**	**JH4**	**41.5**	**ND**	**ND**	**130 000**	**3 600**	**88 000**	**48 000**	**1 700**	**ND**	**40**	**ND**	**2 900**	**ND**	**8.9**	**no-boil**
SD	Mo-vein	a_B4	ND	ND		2 800	770	7 500	7 200	350	ND	5	ND	250	ND	9.1	
Av.	**center**	**JH4**	**36.8**	**468**	**383**	**110 000**	**3 300**	**82 000**	**44 000**	**1 000**	**44**	**44**	**ND**	**2 900**	**3 100**	**36.0**	**boil**
SD	Mo-vein	b_TP1	0.4	2	realPT	3 200	2 000	8 200	1 800	730	17	2	ND	530	460	10.0	
Av.	**center**	**JH4**	**45.7**	**395**	**171**	**130 000**	**3 200**	**100 000**	**65 000**	**1 000**	**75**	**58**	**0.84**	**3 600**	**2 700**	**3.2**	**no-boil**
SD	Mo-vein	b_B2	0.2	2	minPT	6 600	840	16 000	9 900	220	11	17	ND	740	510	0.4	
Av.	**center**	**JH4**	**39.5**	**463**	**354**	**120 000**	**8 500**	**90 000**	**48 000**	**14 000**	**21**	**46**	**1.40**	**3 100**	**2 600**	**69.0**	**no-boil**

SD	Mo-vein	b_B3	1.0	5	minPT	8 700	3 000	22 000	4 800	4 000	7	12	0.65	900	440	23.0	
Av.	**center**	**JH4**	**42.3**	**388**	**168**	**130 000**	**9 300**	**92 000**	**50 000**	**1 200**	**25**	**49**	**ND**	**3 400**	**2 900**	**13.0**	**no-boil**
SD	Mo-vein	b_B4	0.6	1	minPT	5 000	2 700	11 000	7 300	450	ND	0	ND	880	890	ND	
Av.	**center**	**JH4**	**39.0**	**475**	**394**	**110 000**	**5 500**	**95 000**	**34 000**	**780**	**140**	**51**	**0.89**	**3 500**	**3 200**	**3.4**	**no-boil**
SD	Mo-vein	b_B6	ND	ND	minPT	10 000	1 100	25 000	8 500	550	57	19	0.03	490	970	ND	
Av.	**center**	**4990-1470**	**41.8**	**413**	**217**	**120 000**	**7 500**	**84 000**	**34 000**	**2 200**	**24**	**34**	**0**	**2 500**	**2 300**	**7.5**	**no-boil**
SD	Mo-vein	2_B1	0.8	9	minPT	5 300	4 900	13 000	8 200	1 300	7	12	0	390	880	3.0	
Av.	**center**	**4990-1470**	**54.3**	**343**	**ND**	**160 000**	**2 900**	**110 000**	**46 000**	**490**	**78**	**50**	**1**	**3 500**	**2 700**	**16.0**	**no-boil**
SD	Mo-vein	2_B2	0.1	5		4 900	380	12 000	7 100	200	55	6	0	140	240	10.0	
Av.	**center**	**4990-1470**	**51.0**	**362**	**ND**	**150 000**	**4 000**	**98 000**	**45 000**	**5 300**	**50**	**50**	**1**	**3 300**	**3 000**	**5.6**	**no-boil**
SD	Mo-vein	2_B3	0.6	ND		3 000	1 100	6 500	9 600	2 500	26	11	1	420	750	1.1	
Av.	**center**	**4990-1470**	**50.7**	**ND**	**ND**	**150 000**	**3 800**	**110 000**	**47 000**	**2 300**	**61**	**57**	**0**	**3 400**	**3 200**	**5.8**	**no-boil**
SD	Mo-vein	2_B4	ND	ND		4 800	1 700	11 000	7 400	1 000	32	10	0	540	610	4.0	

"deep moly", and "Mo-vein" represent low grade quartz-molybdenite veins, and high grade quartz-molybdenite veins, respectively.

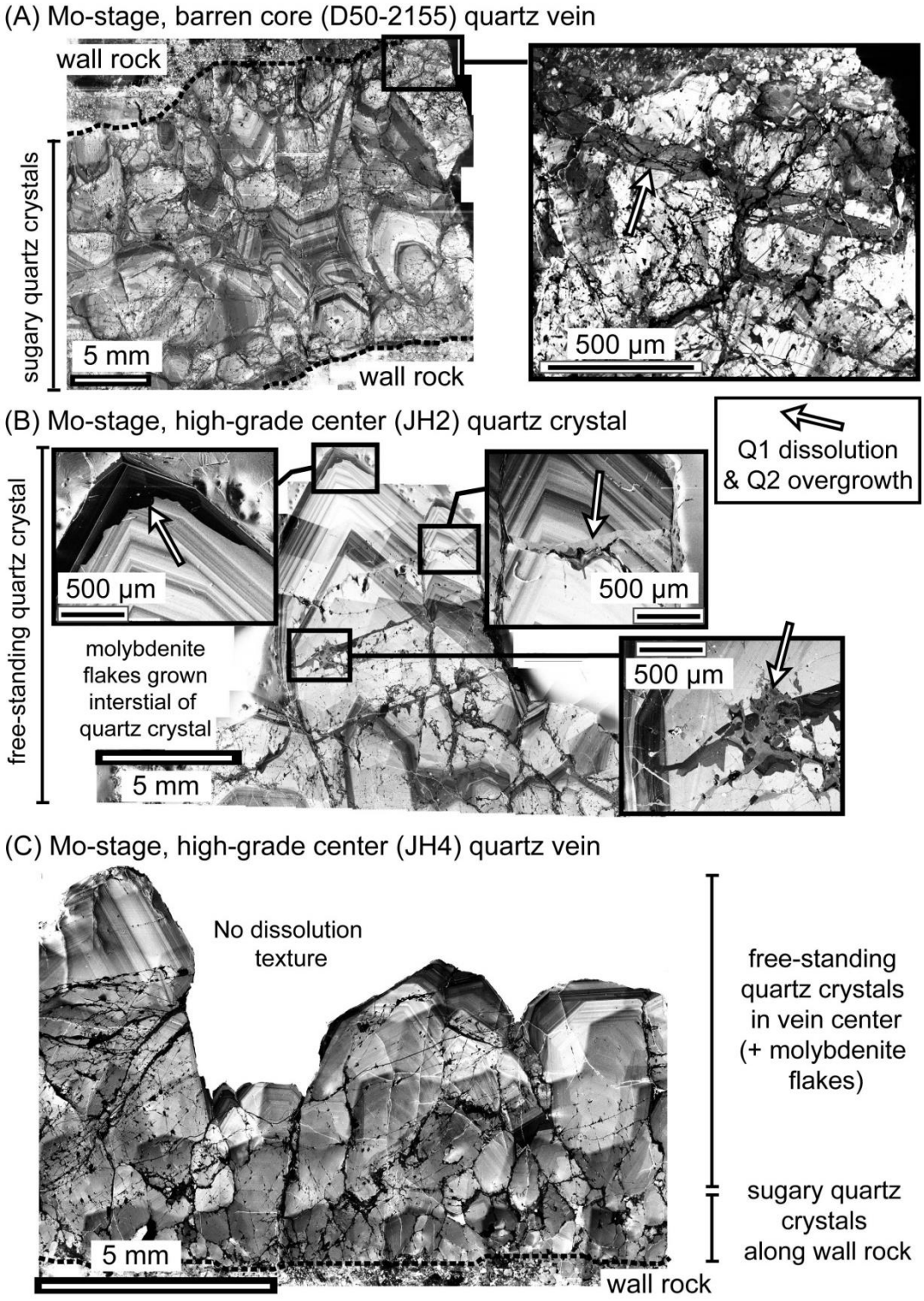

Figure 4. Cathodo-luminescience (CL) images of quartz-molybdenite veins from the low-grade (D50-2155) and high-grade (JH2, JH4) zones. These quartz veins have both euhedral sugary quartz (A) and euhedral free-standing quartz crystals (B, C). Textures of early-generated quartz dissolution (Q1) and second generation quartz overgrowth (Q2) are prominent in the low-grade (A) and high-grade (B) quartz-molybdenite veins. Some quartz-molybdenite veins, however, do not show quartz dissolution textures (C).

In-situ analyses of single fluid inclusions were conducted by laser ablation inductively coupled mass spectrometry (LA-ICP-MS). A beam-homogenized 193 nm ArF Excimer laser ablation system (ETH prototype, similar to Geolas system; Günther et al., 1997) was connected to a quadruple ICP-MS (Perkin Elmer Elan 6100 DRC) optimized for the detection of sulfur as well as metals (Guillong et al., 2008a; Seo et al., 2011). By selection of a reduced set of isotopes to be measured (^{23}Na, ^{29}Si, ^{32}S, ^{39}K, ^{55}Mn, ^{57}Fe, ^{65}Cu, ^{66}Zn, ^{75}As, ^{85}Rb, ^{88}Sr, ^{95}Mo, ^{133}Cs, ^{137}Ba, ^{197}Au and ^{208}Pb) and applying an increased dwell time on selected elements (i.e., 50 ms for ^{197}Au, ^{95}Mo, 20 ms for ^{32}S, and 10 ms for other elements), we reduced the noise of the instrumental backgrounds to improve limits of detection while maintaining the necessary time resolution for representative detection of inclusion signals. We also analyzed ^{55}Mn, ^{66}Zn, ^{85}Rb, ^{88}Sr and ^{137}Ba in some brine inclusion assemblages in order to focus on Fe/Mn ratios. A small amount of H_2 gas (5 ml/min.) added to the He carrier gas increases the sensitivity of selective elements such as Cu, Au, and Mo (Guillong and Heinrich, 2007). Energy densities between 30 and 40 J/cm^2 on the sample surface with 10 Hz pulse frequency allowed controlled sampling of most quartz-hosted fluid inclusions. An Iris aperture was gradually opened during analysis to a spot size allowing complete excavation of the fluid inclusion without the loss of daughter crystals. Quantification followed the data reduction procedures of Günther et al. (1998) and Heinrich et al. (2003) using the SILLS software (Guillong et al., 2008b) for data reduction. Since salinity measurements for the vapor-rich inclusions are difficult, we used element ratios for interpretations of the vapor phase fluids.

We also analyzed some of the intermediate-density and vapor inclusions in quartz veins (A30-3816 and D211-19 in Cu-stage, and D50-2155, 2379, A57-5931, JH2, and JH4 in Mo-stage) by using laser Raman microspectroscopy in ETH Zurich and University of Bern in order to check daughter minerals, and to compare the gas compositions and ratios of CO_2 and CH_4.

Results

Pressure and temperature

Salinities (NaCl equivalent wt %) of brine inclusion assemblages were estimated from halite dissolution temperatures (Bodnar and Vityk, 1994). Some inclusions homogenized by halite dissolution, but most by bubble disappearance, providing estimates of minimum temperature and pressures in the case of brine-only assemblages (Fig. 5). Microthermometric data from brine inclusions in boiling assemblages yield estimates of absolute temperature and pressure of entrapment. True pressures are probably somewhat higher than indicated by the NaCl-H_2O model system (Bodnar and Vityk, 1994; Driesner and Heinrich, 2007) because of the presence of minor CO_2, but also affected by H_2S and other cations indicated by Raman and ICP-MS analyses (Fig. 6). Consistency of homogenization temperatures within brine inclusion assemblages are generally ± 40°C or better (Table 2, 3 and Fig. 5).

The trapping temperature and calculated pressure of the Cu-stage brines obtained from boiling assemblages in low-grade and high-grade quartz stockwork vein samples are from 320 $\pm$ 15 to 430 $\pm$ 7 °C (average $\pm$ 1 σ of fluid inclusion assemblage) and from 90 to 260 bars (Fig. 5), consistent with the previously reported conditions of Cu-Au precipitation at Bingham Canyon (Landtwing et al., 2005; Landtwing et al., 2010). The temperatures and pressures of Mo-stage boiling assemblages extend to significantly higher values than those from the Cu-Au stage fluids, with a maximum of 580 ± 30 °C (Fig. 5) implying a pressure of 710 bar. Brines from boiling assemblages in low Mo grade quartz-molybdenite veins are trapped at temperature from 400 $\pm$ 40 to 500 $\pm$ 8 °C indicating pressures of at least 200–

450 bars (Fig. 5), but possibly higher during the trapping of the predominant intermediate-density inclusions in these deep samples within the single-phase fluid stability field. Brines from boiling assemblages in high Mo grade quartz-molybdenite veins are trapped at temperatures from 360 ± 20 to 580 ± 30 °C indicating pressures of 140–710 bars, comparable ranges to low Mo grade quartz-molybdenite vein samples (Fig. 5). Maximum pressures around 710 bars are consistent with tentative estimations for lithostatic pressure conditions in the barren core during Cu-Au mineralization (Landtwing et al., 2010). Temperatures obtained from boiling assemblages vary from 320 to 430 °C in the Cu-stage fluids, but show a much greater variation from 270 to 580 °C in the Mo-stage fluids, extending to higher temperatures (Fig. 5).

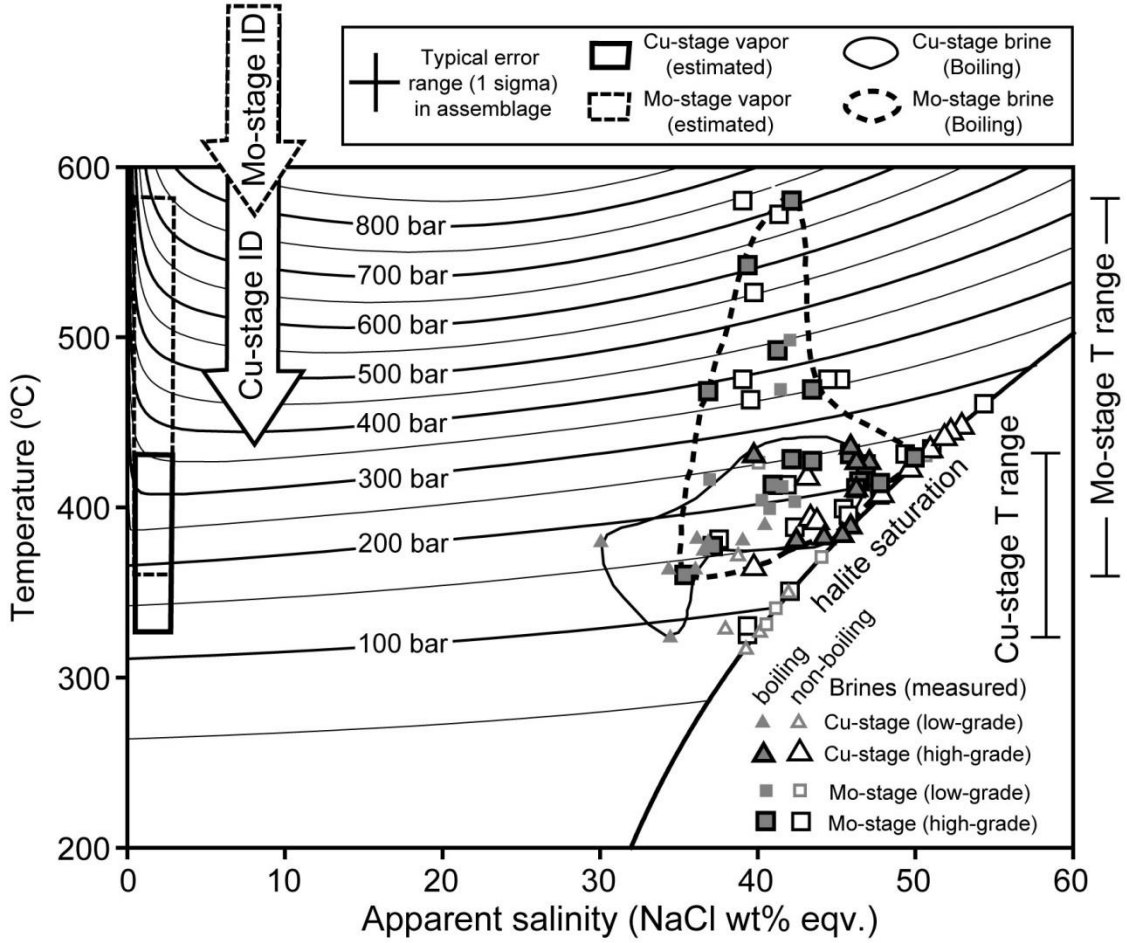

Figure 5. Plots of measured homogenization temperatures (Th; ℃) vs. apparent salinities (NaCl wt% equivalent) in the brine inclusion assemblages of early Cu-stage (quartz stockwork veins) and late Mo-stage (quartz-molybdenite veins). Contours of pressure (bar) were calculated based on the H_2O-NaCl system (Driesner and Heinrich, 2007). Filled symbols represent "boiling assemblage" direct estimations of temperature; Open symbols represent brine-only assemblages of minimum temperature estimations. Among the boiling assemblages in the Cu-stage, brine salinities are higher in the high-grade sample than in the low-grade sample. Comparable brine salinities were found in the Mo-stage samples. Homogenization temperatures in Mo-stage fluids were found to be higher than that in Cu-stage fluids. Typical error ranges in the assemblages are ± 3 wt% and ± 20 °C.

Raman spectroscopy and redox conditions

Gas ratios of CH_4/CO_2 in the intermediate-density and vapor-rich inclusions in quartz stockwork veins (A30-3816 and D211-19) and quartz-molybdenite veins (D50-2155, 2379, A57-5931, JH2, and JH4) were analyzed by Raman spectroscopy at room temperature to

detect trends indicative of redox evolution. However, the low Raman cross-section of CH_4 (Burke, 2001) prevented detection of CH_4 in any intermediate-density or vapor inclusions (Fig. 6). Calculated detection limits for the vapor inclusions in Bingham Canyon deposit, based on the peak areas and background variation of the Raman spectrum and instrumental sensitivities of gas species (Burke, 2001), indicate a maximum CH_4/CO_2 molar ratios of 0.002.

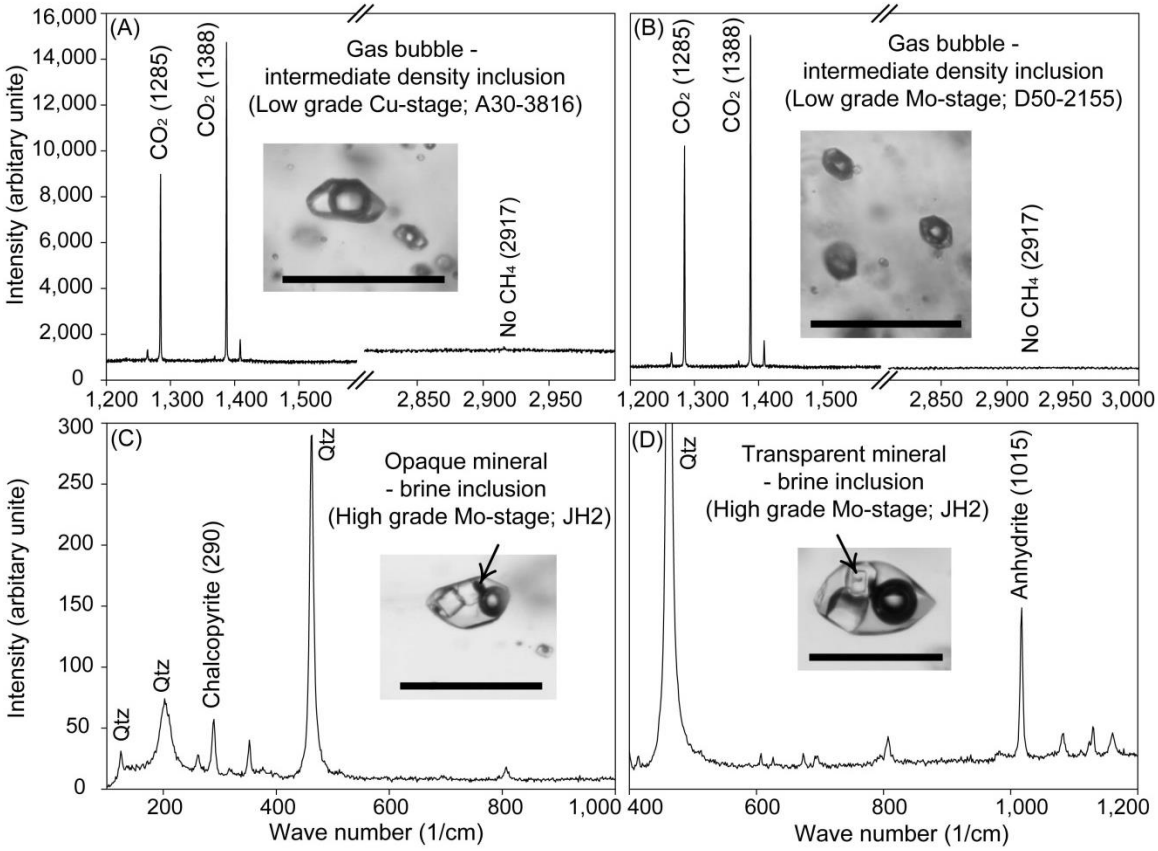

Figure 6. Representative Raman spectrum obtained from bubbles of intermediate-density fluid inclusions from the Cu-stage quartz stockwork (A; A30-3816 sample) and Mo-stage quartz-molybdenite veins (B; D50-2155 sample). These were investigated to check gas species in the intermediate-density fluid inclusions and opaque chalcopyrite and transparent anhydrite daughter crystals in brine inclusions of high Mo grade quartz-molybdenite veins (JH2 sample). The fluid inclusions contain CO_2 but do not contain measurable amounts of CH_4. Calculated detection limits of CH_4/CO_2 molar ratios were near 0.002 corresponding to a log fO_2 near NNO+0.3, suggesting that CH_4 detection is difficult in oxidized fluids of log fO_2 higher than NNO+0.3. The precipitated sulfide (chalcopyrite) and sulfate (anhydrite) daughter crystals do not allow accurate determination of oxidized/reduced sulfur species ratios in the fluids. Scale bars in inclusion images are 100 μm.

Fluid compositional variations

Salinities of brines range from 31 ± 1 to 42 ± 1 wt % NaCl eq. (average $\pm 1\sigma$; 38 ± 3 wt %) in the deep low Cu grade quartz stockwork veins, and from 40 ± 1 to 54 ± 2 wt % NaCl eq. (average; 48±4 wt %) in the high Cu grade quartz stockwork veins of the Cu-Au orebody (Fig. 5 and Table 2). The salinity increase in the Cu-stage is consistent with the salinity evolution in the central upflow zone documented by Landtwing et al. (2010). In the late-stage stockwork vein (post-QLP; 4990-1470 sample), salinities of two brine assemblages (40 ± 1 and 44 ± 1 wt % NaCl eq.) are similar to brine assemblages in the high Cu grade stockwork veins. Salinities of brines in low Mo grade quartz-molybdenite veins vary from 37 ± 1 to 51 ± 1 wt % NaCl eq. (average; 42 ± 3 wt %) and in the high Mo grade quartz-molybdenite veins range from 36 ± 1 to 59 ± 2 wt % NaCl eq. (average; 44 ± 5 wt %; Fig. 7

and Table 3). There is a slight trend of increasing salinity from the deep low-grade veins of the Mo-stage to the rich quartz-molybdenite veins, but overall the salinities of the Mo-stage brines overlap with those of the Cu-Au-stage (Fig. 5 and 7).

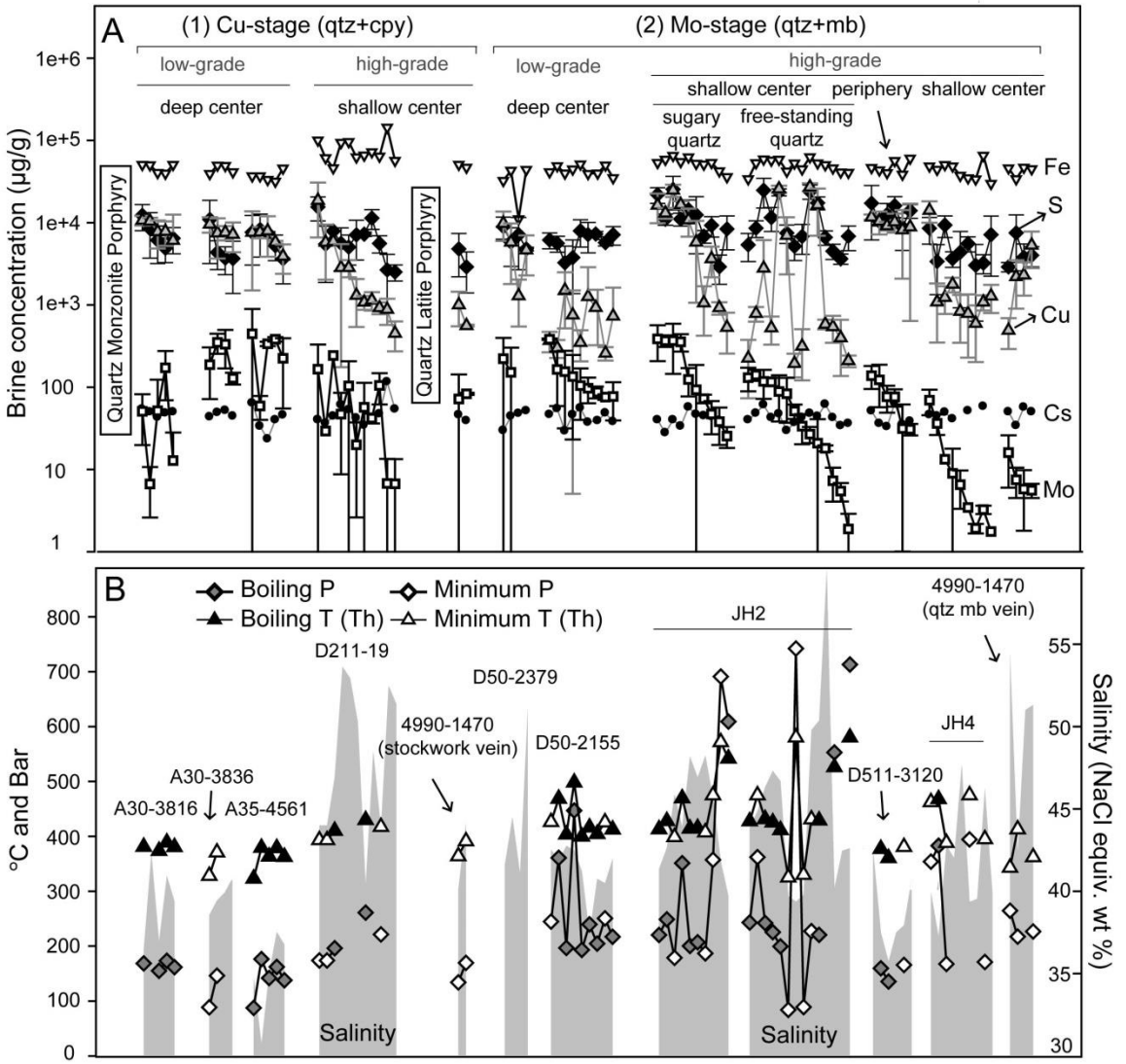

Figure 7. Microthermometry and LA-ICP-MS microanalysis of brine inclusion assemblages from Bingham Canyon. (A) Concentrations of Fe, Cu, Cs, Mo, and S in the brine inclusion assemblages in low Cu grade quartz stockwork veins in the barren core (A30-3816, A30-3836, and A35-4561), high Cu grade quartz stockwork vein (D211-19), post-QLP quartz stockwork vein (4990-1470), low Mo grade quartz-molybdenite veins in the barren core (D50-2155 and D50-2379) and high Mo grade quartz-molybdenite veins [JH2 (early sugary quartz and late free-standing quartz; Fig. 3B) D511-3120, JH4, and 4990-1470]. Error bars of S, Cu, and Mo represent one standard deviation in the assemblages. Since these quartz veins contain chalcopyrite (cpy) and molybdenite (mb), the Cu-stage (1) and Mo-stage assemblages (2) were sorted by Cu/Na and Mo/Na ratios, respectively. (B) Measured homogenization temperatures (℃; T_h), salinities (wt% NaCl eqv.), and calculated pressures (bars) of the brine assemblages. Closed symbol represent "boiling assemblage" direct estimations of P-T; Open symbols are from brine-only assemblages representing minimum estimations of P-T.

Consistent copper concentrations within brine inclusion assemblages from the low Cu grade quartz stockwork veins vary from 4,000 ± 1,400 to 11,000 ± 1,400 µg/g (average; 8,600 ± 3,200 µg/g). In each assemblage, they are approximately matched by S contents ranging between 3,600 ± 1,800 and 12,000 ± 4,300 µg/g (average 7,000 ± 3,000 µg/g; Fig. 7). In the low Mo grade quartz-molybdenite veins, however, S concentrations from 3,300 ± 1,900 to

9,000 ± 2,700 μg/g (average; 6,000 ± 1,500 μg/g) in brines are variably and sometimes significantly higher than Cu concentrations that range from 260 ± 48 to 9,800 ± 3,800 μg/g (average 700 ± 400 μg/g). Mo concentrations in low-grade veins from both Cu- and Mo-stages are comparable, from 7 ± 4 to 380 ± 24 μg/g (average 180 ± 150 μg/g) in low Cu grade quartz stockwork veins and from 80 ± 6 to 380 ± 9 μg/g (average 140 ± 90 μg/g) in low Mo grade quartz-molybdenite veins. Fe/Mn atomic ratios in brines from the low Cu grade stockwork veins between 3.7 ± 1.2 and 7.3 ± 0.4 are generally lower than those in the low Mo grade quartz-molybdenite veins which vary from 5.3 ± 0.4 to 12.0 ± 2.1 (Fig. 9 and Table 4).

In high Cu grade quartz stockwork veins (D211-19), Cu concentrations in the brines vary from 450 ± 180 to 19,000 ± 12,000 μg/g and S concentrations in the brines are from 2,500 ± 550 to 16,000 ± 5,000 μg/g. The parallel decreases of Cu with S are consistent with previously analyzed fluid inclusions in the same sample (D211-19) interpreted to be caused by Cu-sulfide precipitation with falling temperature (Landtwing et al., 2005; Landtwing et al., 2010). Molybdenum concentrations in the high Cu grade quartz stockwork vein are from 7 ± 7 to 360 μg/g, in a similar range to low-grade quartz veins from Cu- and Mo-stages. Two brine inclusion assemblages in late-stage quartz stockwork vein (post-QLP; 4990-1470) contain 560 ± 14 and 1,000 ± 450 μg/g of Cu, 2,900 ± 1,500 and 4,800 ± 2,600 μg/g of S, and 72 ± 70 and 83 ± 2 μg/g of Mo (Table 2).

In the high Mo grade quartz-molybdenite vein (JH2 sample; Fig. 7), we observed wide variations of Mo contents (between 2 ± 1 and 390 ± 180 μg/g) in the brines. In sample JH2, brines in the early sugary quartz with microcrystalline molybdenite contain from 25 ± 7 to 390 ± 180 μg/g, and brines in the euhedral quartz that intergrown with flakes of molybdenite contain overlapping, but generally lower Mo from 2 ± 1 to 140 ± 22 μg/g (Fig. 7).

Despite relatively low concentrations of Cu in all Mo-stage quartz veins (Fig. 7), a few brine assemblages contain extremely enriched Cu and S concentrations in the confined P-T ranges around 420℃ and 210 bars (Fig. 7), while maintaining relatively constant Pb concentrations of 3,000 ± 200 μg/g. Generally, the concentrations of non-precipitating elements such as Pb, Zn and Cs are constant throughout all fluid stages, especially if normalized to Na (Table 2 and 3).

Compositional trends of vapor inclusions from the Bingham Canyon deposit are similar to the brines (Fig. 8 and Table 5). Intermediate-density inclusion assemblages in the low Cu grade quartz stockwork veins have comparable S (S/Na; from 0.22 to 0.88) and Cu (Cu/Na; from 0.07 to 0.32) contents with some Mo (Mo/Na; from 0.0004 to 0.0054). Intermediate-density inclusion assemblages in the low Mo grade quartz-molybdenite veins contain variable excess of S (S/Na; from 0.11 to 0.28) relative to Cu (Cu/Na; from 0.01 to 0.11) with some Mo (Mo/Na; from 0.0007 to 0.0018; Fig. 8). We observed wide variations of Mo/Na ratios (from 0.0001 to 0.0110) in the intermediate-density and vapor inclusion assemblages of high Mo grade quartz-molybdenite veins (A57-6093, JH2, and 4990-1470), similar trends were observed in brines from the same samples.

Cogenetic vapor and brine phase fluids (boiling assemblages) are shown in Figure 11, emphasizing the variable tendency of Mo, As, Au, Cu and S enrichment in the vapor inclusions, compared with the salt components Fe, Cs, K and Na. Quartz-hosted vapor + brine inclusion pairs from the Cu-stage and the Mo-stage at Bingham Canyon are compared, as well as data of some Sn-W granites where both S and Mo data are available (Seo et al., 2009; Landtwing et al., 2010). All elements were normalized to the analytically robust Pb concentration (accurate, precise, and little change of v/b partitioning). The data show that Mo selectively fractionates into vapor relative to chloride salts in the Sn-W-systems and to a lesser but significant degree in the Mo-stage fluids at Bingham Canyon, whereas brine +

vapor pairs from the Cu-Au-stage show no significant preferential partitioning or a tendency for Mo to favor the brine phase.

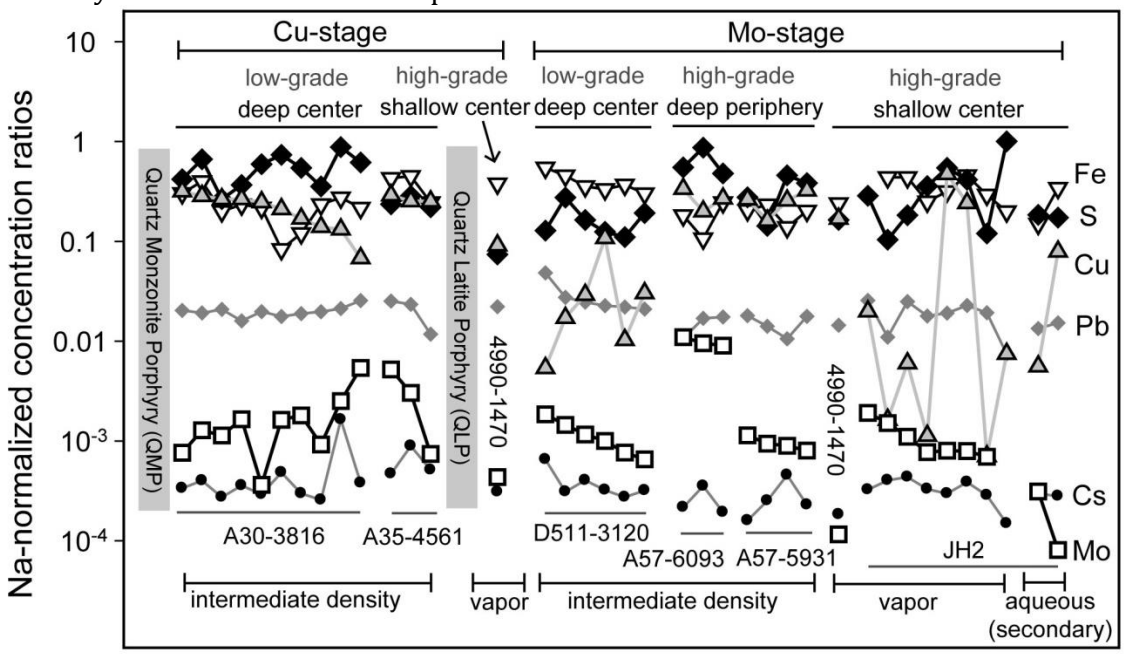

Figure 8. Na-normalized ratios of Fe, Cu, Mo, Cs, Pb, and S in the intermediate-density, vapor, and late aqueous inclusion assemblages in low Cu grade quartz stockwork veins (A30-3816 and A35-4561), post-QLP (Quartz Latite Porphyry) late-stage quartz stockwork vein (4990-1470), low Mo grade quartz-molybdenite vein (D50-2155), deep peripheral high Mo grade quartz-molybdenite veins (A57-5931, 6093), and shallow high Mo grade quartz-molybdenite veins (JH2 and 4990-1470). We used analytically robust element ratios since it is difficult to obtain accurate element concentrations of these low-salinity fluid inclusions. The assemblages of Cu-stage and Mo-stage are sorted by Cu/Na and Mo/Na ratios, respectively.

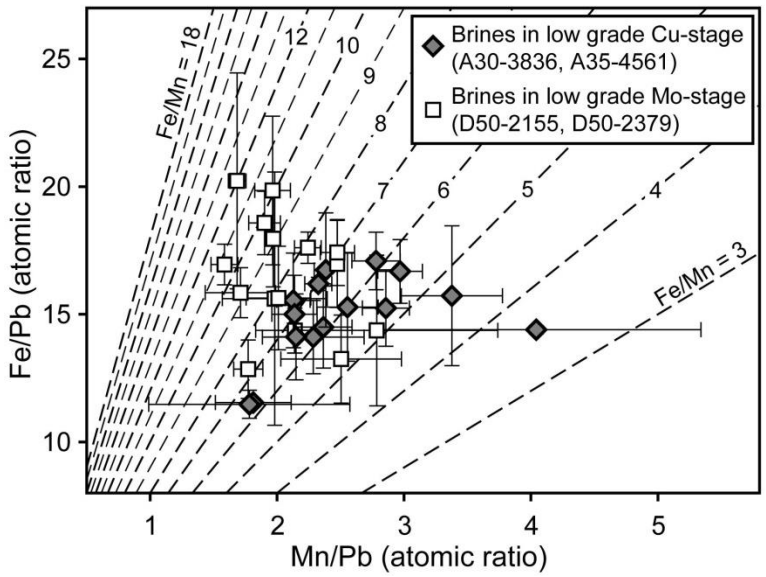

Figure 9. Fe/Pb and Mn/Pb ppm ratios measured in brine assemblages of low grade Cu quartz stockwork veins (A30-3836, A35-4561) and low grade quartz-molybenite veins (D50-2155, 2379) from the barren core. Contours of Fe/Mn ratios from 3 to 18 are presented. Fe/Mn ratios of the Cu-stage range from 3.7 ± 1.2 to 7.3 ± 0.4, lower than that of the Mo-stage range, from 5.3 ± 0.4 to 12.0 ± 2.1. Error bars represent one standard deviation in the assemblages.

Table 5. Compostion of intermediate density (ID), vapor, and late aqueous fluid inclusion assemblages.

µg/g	Location	Phase	Sample#	Sal.	Th(°C)	P(bar)	^{23}Na	^{32}S	^{39}K	^{57}Fe	^{65}Cu	^{75}As	^{133}Cs	^{197}Au	^{208}Pb	^{66}Zn	^{95}Mo
Av.	**center**	**ID**	**A35-4561**	**9.8**	**330**		**26 000**	**6 200**	**12 000**	**11 000**	**7 600**	**50**	**12.0**	**0.44**	**660**	**ND**	**130**
SD	**deep stw.**		1_ID1	ND			6 400	3 900	7 500	5 900	6 100	36	4.9	0.26	280	ND	210
Av.	**center**	**ID**	**A35-4561**	**6.2**			**16 000**	**4 700**	**8 400**	**7 500**	**4 200**	**50**	**14.0**	**0.64**	**390**	**ND**	**50**
SD	**deep stw.**		1_TP2(v)	1.1			3 600	3 000	4 000	2 900	2 600	57	30.0	1.10	240	ND	45
Av.	**center**	**ID**	**A30-3816**	**8**	**381**	**168**	**23 000**	**9 800**	**20 000**	**7 100**	**7 400**	**47**	**7.9**	**0.21**	**470**	**490**	**17**
SD	**deep stw.**		4_TP11(v)	assum			77	1 800	190	1 300	3 300	16	0.8	0.17	36	49	12
Av.	**center**	**ID**	**A30-3816**	**8**			**25 000**	**6 700**	**14 000**	**5 100**	**6 700**	**42**	**7.0**	**0.44**	**530**	**600**	**29**
SD	**deep stw.**		1_ID12	assum			670	2 000	1 700	2 200	2 100	10	1.6	ND	110	95	23
Av.	**center**	**ID**	**A30-3816**	**8**			**25 000**	**15 000**	**14 000**	**5 500**	**6 300**	**93**	**7.5**	**3.00**	**500**	**690**	**9**
SD	**deep stw.**		1_ID6	assum			1 100	5 900	3 200	790	1 500	96	2.5	ND	190	200	3
Av.	**center**	**ID**	**A30-3816**	**8**			**23 000**	**8 600**	**20 000**	**5 500**	**6 200**	**56**	**8.4**	**ND**	**370**	**420**	**39**
SD	**deep stw.**		1_ID5	assum			990	3 700	2 700	680	150	25	3.5	ND	63	100	27
Av.	**center**	**ID**	**A30-3816**	**8**	**380**	**162**	**25 000**	**18 000**	**14 000**	**2 100**	**5 300**	**34**	**12.0**	**0.44**	**450**	**530**	**41**
SD	**deep stw.**		4_TP9(v)	assum			970	13 000	2 400	2 000	5 600	15	7.8	0.45	180	270	25
Av.	**center**	**ID**	**A30-3816**	**6.2**	**496**		**17 000**	**11 000**	**10 000**	**7 000**	**5 000**	**73**	**7.1**	**5.40**	**340**	**ND**	**22**
SD	**deep stw.**		1_ID1	ND			1 900	5 000	1 200	1 900	3 100	54	1.3	5.60	140	ND	8
Av.	**center**	**ID**	**A30-3816**	**8**			**25 000**	**13 000**	**16 000**	**3 000**	**4 200**	**73**	**7.4**	**0.16**	**470**	**500**	**45**
SD	**deep stw.**		1_ID3	assum			1 200	6 700	3 400	1 600	1 800	45	2.4	ND	170	190	41
Av.	**center**	**ID**	**A30-3816**	**8**			**24 000**	**8 700**	**17 000**	**5 700**	**3 400**	**46**	**6.3**	**0.11**	**480**	**460**	**22**
SD	**deep stw.**		1_ID4	assum			1 000	5 500	2 500	3 000	2 800	25	3.1	0.11	210	190	16
Av.	**center**	**ID**	**A30-3816**	**8**	**374**	**155**	**23 000**	**14 000**	**19 000**	**5 100**	**1 600**	**38**	**8.9**	**0.24**	**600**	**900**	**120**
SD	**deep stw.**		4_TP10(v)	assum			450	11 000	1 800	6 900	1 800	25	0.6	ND	190	590	92
Av.	**center**	**ID**	**A30-3816**	**3.3**	**375**		**9 300**	**8 100**	**6 800**	**2 500**	**1 200**	**250**	**15.0**	**8.50**	**190**	**ND**	**23**
SD	**deep stw.**		1_ID2	ND			800	6 300	1 300	1 300	530	400	15.0	8.40	96	ND	13
Av.	**center**	**vapor**	**4990-1470**	**8**	**ND**	**ND**	**23 000**	**1 700**	**17 000**	**8 700**	**2 100**	**14**	**7.1**	**0.07**	**510**	**630**	**10**
SD	**QLP stw.**		1_V1	assum			570	460	1 000	2 200	1 700	9	2.1	0.04	8	160	10
Av.	**center**	**ID**	**D50-2155**	**8**	**498**	**447**	**22 000**	**2 800**	**21 000**	**12 000**	**120**	**ND**	**14.0**	**ND**	**1 000**	**1 100**	**41**

SD	**deep moly**		A05(v)	assum			ND	ND	ND	ND	ND	ND	ND	ND	ND	ND	ND
Av.	**center**	**ID**	**D50-2155**	**8**	**416**	**240**	**24 000**	**6 600**	**18 000**	**10 000**	**410**	**21**	**7.4**	**0.18**	**660**	**620**	**35**
SD	**deep moly**		B03(v)	assum			740	4 400	1 800	9 300	850	22	2.2	0.14	160	150	54
Av.	**center**	**ID**	**D50-2155**	**8**	**399**	**193**	**23 000**	**3 800**	**20 000**	**8 200**	**670**	**24**	**9.3**	**0.21**	**570**	**720**	**26**
SD	**deep moly**		B06(v)	assum			3 900	1 400	9 900	4 200	680	29	4.9	0.09	150	590	18
Av.	**center**	**ID**	**D50-2155**	**8**			**24 000**	**2 900**	**18 000**	**7 900**	**2 500**	**11**	**7.7**	**0.48**	**540**	**590**	**24**
SD	**deep moly**		A01(v)	assum			490	1 300	1 100	790	1 400	4	1.0	0.46	110	200	8
Av.	**center**	**ID**	**D50-2155**	**8**	**404**	**205**	**23 000**	**2 600**	**19 000**	**8 700**	**240**	**9**	**6.5**	**0.09**	**520**	**640**	**18**
SD	**deep moly**		B01(v)	assum			570	1 500	1 500	1 500	210	6	3.3	0.01	95	57	11
Av.	**center**	**ID**	**D50-2155**	**8**	**412**	**217**	**24 000**	**4 600**	**18 000**	**7 200**	**720**	**10**	**7.7**	**0.11**	**500**	**430**	**15**
SD	**deep moly**		B02(v)	assum			700	3 200	1 700	1 300	920	4	1.5	0.05	100	140	9
Av.	**periphery**	**ID**	**A57-5931**	**8**			**28 000**	**13 000**	**7 400**	**3 900**	**7 200**	**75**	**12.0**	**1.30**	**290**	**430**	**25**
SD	**Mo-vein**		ID1	assum			680	6 100	1 600	1 500	1 700	70	9.5	ND	94	200	25
Av.	**periphery**	**ID**	**A57-5931**	**8**			**27 000**	**7 600**	**9 100**	**5 600**	**7 200**	**38**	**4.4**	**0.54**	**490**	**550**	**31**
SD	**Mo-vein**		ID2	assum			600	1 000	1 600	1 600	1 600	14	0.5	ND	63	91	15
Av.	**periphery**	**ID**	**A57-5931**	**8**			**27 000**	**10 000**	**10 000**	**5 500**	**8 800**	**49**	**6.2**	**0.89**	**480**	**550**	**21**
SD	**Mo-vein**		ID3	assum			190	2 600	420	1 000	2 200	12	2.2	0.53	140	110	13
Av.	**periphery**	**ID**	**A57-5931**	**8**			**28 000**	**4 000**	**8 200**	**6 500**	**4 500**	**29**	**7.0**	**1.00**	**390**	**480**	**26**
SD	**Mo-vein**		ID4	assum			1 700	1001	4 500	2 400	1 300	13	3.3	0.18	130	200	10
Av.	**periphery**	**ID**	**A57-6093**	**8**			**28 000**	**15 000**	**7 300**	**5 100**	**9 500**	**80**	**6.1**	**3.30**	**300**	**460**	**310**
SD	**Mo-vein**		ID1	assum			530	4 000	1 500	2 500	2 800	10	2.8	ND	57	140	400
Av.	**periphery**	**ID**	**A57-6093**	**8**			**27 000**	**23 000**	**9 600**	**2 900**	**5 400**	**68**	**9.6**	**1.30**	**460**	**660**	**260**
SD	**Mo-vein**		ID2	assum			760	7 000	2 300	1 700	1 500	54	3.8	ND	16	220	34
Av.	**periphery**	**ID**	**A57-6093**	**8**			**28 000**	**13 000**	**7 300**	**6 900**	**7 500**	**51**	**5.4**	**ND**	**490**	**610**	**250**
SD	**Mo-vein**		ID3	assum			490	3 000	1001	1 400	1 500	28	3.1	ND	77	120	ND
Av.	**center**	**vapor**	**JH2**	**8**			**25 000**	**7 200**	**14 000**	**ND**	**500**	**ND**	**8.2**	**ND**	**650**	**490**	**48**
SD	**Mo-vein**		8-1_V3	assum			ND	ND	ND	ND	ND	ND	ND	ND	ND	ND	ND
Av.	**center**	**vapor**	**JH2**	**8**			**26 000**	**2 700**	**13 000**	**11 000**	**42**	**20**	**10.0**	**1.70**	**280**	**660**	**39**
SD	**Mo-vein**		8-1_V2	assum			970	ND	2 500	ND	ND	ND	0.3	ND	340	ND	ND

Av.	**center**	**vapor**	**JH2**	**8**			**20 000**	**3 600**	**18 000**	**8 800**	**120**	**16**	**8.7**	**0.11**	**500**	**590**	**22**
SD	**Mo-vein**		2_V2	assum			3 400	2 900	5 400	3 800	93	20	4.2	0.07	190	310	22
Av.	**center**	**vapor**	**JH2**	**8**			**25 000**	**8 900**	**16 000**	**6 200**	**28**	**36**	**8.2**	**1.10**	**440**	**320**	**19**
SD	**Mo-vein**		3-1_V1	assum			330	ND	900	4 200	22	42	1.8	ND	33	3	15
Av.	**center**	**vapor**	**JH2**	**7.9**	**429**	**221**	**22 000**	**12 000**	**13 000**	**7 200**	**10 000**	**25**	**6.7**	**1.30**	**430**	**ND**	**18**
SD	**Mo-vein**		a7(v)	3.2			8 300	10 000	5 600	5 100	10 000	12	4.3	ND	240	ND	19
Av.	**center**	**vapor**	**JH2**	**8**			**20 000**	**8 400**	**17 000**	**9 300**	**4 900**	**22**	**7.9**	**0.17**	**460**	**590**	**16**
SD	**Mo-vein**		2_V1	assum			4 600	7 500	6 600	4 700	8 200	33	5.0	0.08	180	390	10
Av.	**center**	**vapor**	**JH2**	**8**			**22 000**	**2 600**	**15 000**	**6 500**	**15**	**20**	**6.3**	**0.13**	**430**	**430**	**15**
SD	**Mo-vein**		2_V3	assum			930	2 000	1 400	1 900	6	18	1.0	0.10	41	69	8
Av.	**center**	**vapor**	**JH2**	**8**			**26 000**	**26 000**	**12 000**	**5 300**	**190**	**79**	**3.9**	**0.90**	**190**	**480**	**ND**
SD	**Mo-vein**		8-1_V1	assum			610	7 600	1 600	210	49	29	1.9	ND	150	98	ND
Av.	**center**	**vapor**	**JH2**	**7.4**	**492**	**434**	**22 000**	**5 400**	**11 000**	**7 000**	**300**	**150**	**9.3**	**3.70**	**540**	**ND**	**21**
SD	**Mo-vein**		B_BT2	3.1			3 800	2 500	3 400	1 800	240	29	6.9	2.90	470	ND	ND
Av.	**center**	**vapor**	**4990-1470**	**8**	**ND**	**ND**	**25 000**	**4 100**	**13 000**	**6 000**	**4 200**	**38**	**4.6**	**ND**	**360**	**430**	**3**
SD	**Mo-vein**		2_V1	assum			850	2 900	1 800	3 300	4 300	ND	0.4	ND	55	45	ND
Av.	**center**	**aqueous**	**JH2**	**9.7**	**313**	**97**	**30 000**	**5 600**	**15 000**	**4 500**	**170**	**69**	**9.1**	**6.00**	**410**	**690**	**10**
SD	**Mo-vein**		a8-2_AQ	ND			1 700	2 600	2 500	4 500	ND	44	2.4	6.80	170	360	3
Av.	**center**	**aqueous**	**JH2**	**8**			**25 000**	**4 300**	**15 000**	**8 600**	**1 900**	**ND**	**7.0**	**ND**	**380**	**450**	**2**
SD	**Mo-vein**		3-1_AQ1	assum			ND	ND	ND	ND	ND	ND	ND	ND	ND	ND	ND

Due to difficulties to get reliable salinities from such low-density inclusions, most of the intermediate density (ID) and vapor phase salinities were assumed as 8 equiv. NaCl wt % based on previous estimations (Redmond et al., 2004; Landtwing et al., 2010). Only element ratios are analytically-robust and are therefore reported in the current text. Temperatures, pressure data for some vapor inclusions were obtained from brine inclusion data in boiling assemb lages.

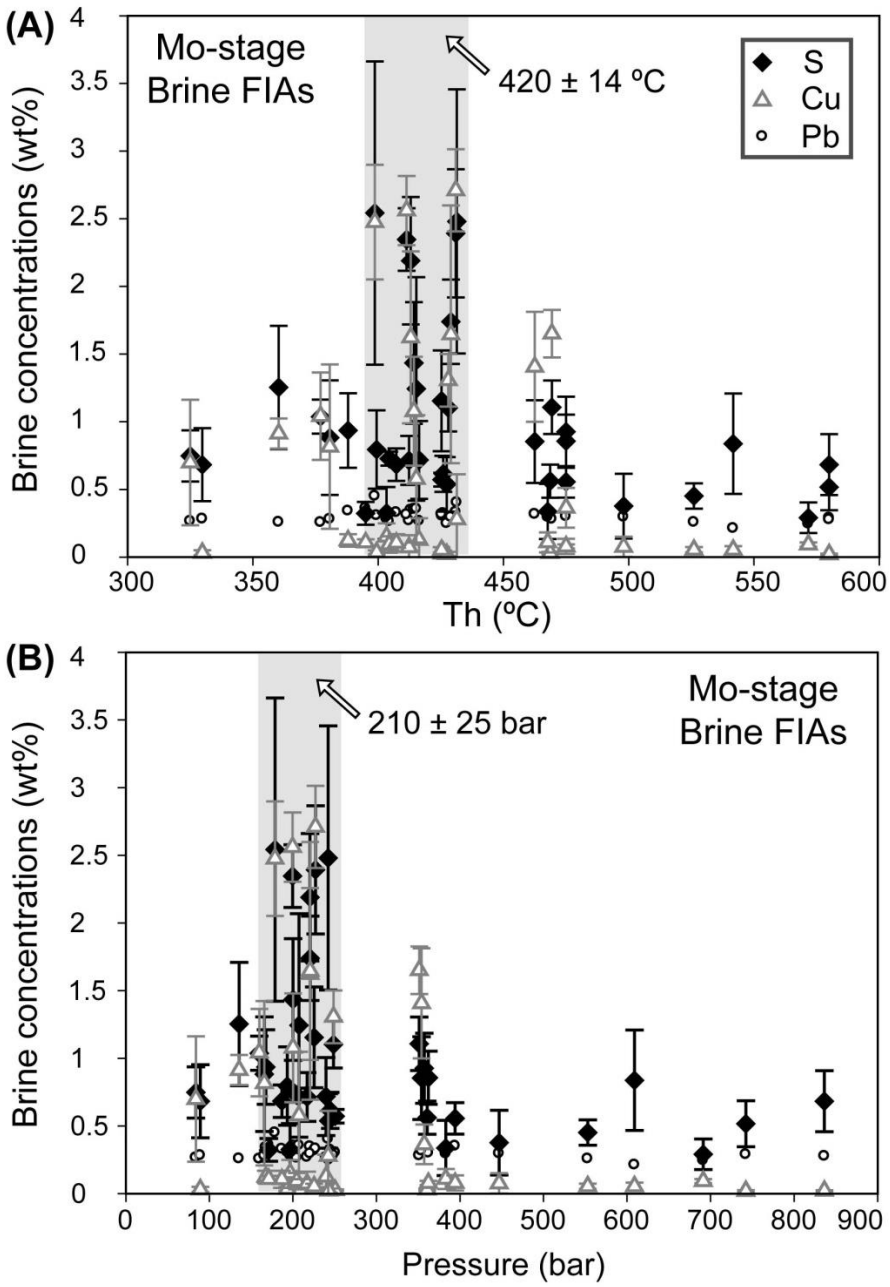

Figure 10. Cu, Pb, and S concentrations vs. homogenization temperatures (A) and estimated pressures (B) in the brine fluid inclusion assemblages (FIAs) in the quartz-molybdenite veins, with error bars of Cu and S concentrations (1 standard deviation in each assemblage). Anomalously high concentrations of Cu and S are confined to ranges of temperature (400-430 °C; **A**) and pressure (150-250 bars; **B**) where retrograde quartz solubility favors access of the Mo-stage fluids to re-dissolve Cu-Fe-sulfide grains that were precipitated in the preceding Cu-Au stage.

Discussion

The presence of intermediate-density inclusions in the deep, low grade quartz-molybdenite veins, and brine and vapor inclusions in the shallow high grade quartz-molybdenite veins, are interpreted to indicate phase separation of a single-phase fluid ascending from depth. From the combined studies of quartz vein textures, fluid inclusion microthermometry, and LA-ICP-MS results, we found only minor differences between the distinct Cu- and Mo-stages

with regard to the metal and sulfur contents of the fluids, the prevailing P-T conditions of mineralization, and the evolution of fluids from single-phase intermediate-density to high-density brine and low-density vapor. The differences may imply that the sharply contrasting metal content of the two vein stages reflects selective metal deposition rather than major differences in fluid characteristics. We argue in the followings that metal separation may be explained by a rather subtle change towards more reducing and possibly acidic conditions in the magmatic fluid source. In addition, local redissolution of earlier ore minerals by later fluids and an unknown degree of post-entrapment diffusional reequilibration may have added to the compositional complexity of the fluid inclusion assemblages.

Magmatic metal fractionation and source magma evolution

Molybdenum is an incompatible element in a crystallizing magma (Candela and Holland, 1984; Keppler and Wyllie, 1991), so that fractional crystallization accumulates Mo in the residual melt (Audétat, 2010). As a result later stage magma is expected to exsolve the most Mo-rich fluids. Fluid-conservative elements including Cs, Pb, and Zn are also incompatible during magmatic fractionation (Audétat and Pettke, 2003) but do not precipitate as distinct mineral phases in the core of porphyry deposits. Concentrations of these elements in the fluids do not change significantly from the Cu- to the Mo-stage at Bingham Canyon, and Pb isotope ratios in the fluid inclusions show that the fluids responsible for the Cu and Mo stage ores in the Bingham Canyon deposit originated from the same magmatic source (Pettke et al., 2010). These observations argue against fundamental differences in source magmas or a highly contrasting degree of magma fractionation, as a cause for the distinct metal endowments of the two mineralization stages at Bingham Canyon. Indeed, the Mo-stage fluids are not more Mo-rich, but they tend to be depleted in Cu, which is also incompatible in the magma but might be removed by early-exsolving, S-rich magmatic vapor phase (Zajacz and Halter, 2009). Copper depletion with continued high Mo supply could therefore reflect a process of metal segregation during progressive fluid separation from a single, progressively crystallizing magma reservoir.

P-T conditions and extent of phase separation

The temperature and pressure of late Mo stage fluids of a maximum of 580 °C with an estimated pressure of up to 710 bar (Fig. 5) overlap with the maximum pressure around 500 °C and 800 bars for Cu-Au stage fluids from barren core estimated by Landtwing et al. (2010), suggesting that the P-T conditions of the deep input intermediate-density phase fluids of the two ore-forming stages (Cu and Mo) were essentially constant within our observational uncertainty. The salinity ranges of brines in both ore stages overlap as well (Fig. 5), indicating that single phase fluids in early Cu- to late Mo-stages decompressed and cooled, and underwent similar extents of brine + vapor phase separation. Following the mass-balance approach of Landtwing et al. (2010) using fluid salinity and analyzed element ratio with the 'lever rule' applied to H_2O-NaCl model system (Driesner and Heinrich, 2007), we calculated the mass fractions of the brine and vapor in the system responsible for the Mo-stage by using the observed salinities and element ratios. The element/Na ratios of intermediate-density fluid inclusion assemblages in low-grade sample (D50-2155) and two boiling assemblages in shallow high-grade samples (JH2_a7 and BT2; Seo et al., 2009) were taken as representative to estimate the mass fractions of separating vapor and brine in the Mo-stage fluid plume (Table 6). For the calculation, we assumed the initial salinity of the intermediate-density fluids as 8 wt % NaCl equiv. based on previous estimates (Redmond et al., 2004; Landtwing et al., 2010). The element ratios in the intermediate-density fluids, and the salinities and element ratios in the brines in the boiling assemblages are adopted to predict the salinity and element ratios of the coexisting vapor inclusions in the boiling

Table 6. Mass-balance calculation to estimate vapor composition and vapor-brine mass fractions.

		Intermediate-density Analyzed (average all ID)		Brine in boiling assemblage Analyzed (JH2_BT2)			Calculated vapor (100g ID fluid — X * 100g Brine)			Vapor in boiling assemblage Analysed (JH2_BT2)		
			Salinity		Salinity			Salinity		Salinity		
			wt % NaCl eq.		wt % NaCl eq.	Fluid Mass		wt % NaCl eq.	Fluid Mass	wt % NaCl eq.	Error (1 σ)	
			8.0		**41.7**	Fraction:		4.5	Fraction:	**7.4**	**3.1**	**3.1**
		Na wt % =	*2.1*	Na wt% =	*11.6*	**0.1**	Na wt% =	*1.1*	0.9			
Com-	*mMCl/mM*	Ratios	Conc. wt %	Ratios	Conc. wt%	Comp.	Ratios	Conc. wt%	Comp.	El-Ratio	Error (1 σ)	
ponent		M/Na (ICP)	(gMCl/100g ID)	M/Na (ICP)	(gMCl /100g B)	Fraction	M/Na (pred)	(gMClx/100gV)	Fraction	M/Na (ICP)	+	–
(a)	(b)	(c)	(d)	(e)	(f)	(g)	(h)	(i)	(k)	(l)	(m)	(n)
NaCl	2.54	**1**	5.345	**1**	29.428	2.943	1	2.670	2.403	**1**	**0**	**0**
KCl	1.91	**0.840**	3.368	**0.684**	15.089	1.509	1.032	2.065	1.859	**0.522**	**0.158**	**0.158**
$FeCl_2$	2.27	**0.390**	1.861	**0.340**	8.924	0.892	0.452	1.077	0.969	**0.324**	**0.084**	**0.084**
S	1	**0.170**	0.357	**0.053**	0.609	0.061	0.314	0.329	0.297	**0.266**	**0.164**	**0.164**
Cu	1	**0.033**	0.069	**0.011**	0.122	0.012	0.061	0.064	0.057	**0.016**	**0.017**	**0.016**
$PbCl_2$	1.34	**0.028**	0.079	**0.034**	0.526	0.053	0.021	0.029	0.026	**0.026**	**0.023**	**0.023**
Mo	1	**1.10E-03**	2.31E-03	**7.95E-04**	9.20E-03	9.20E-04	1.47E-03	1.55E-03	1.39E-03	**8.65E-04**		
Au	1	**1.00E-05**	2.10E-05	**1.14E-05**	1.32E-04	1.32E-05	8.27E-06	8.68E-06	7.81E-06	**1.80E-04**	**0.0001**	**0.0001**
As	1	**0.0005**	0.0011	**0.0004**	0.0050	0.0005	0.0007	0.0007	0.0006	**0.0068**	**0.0014**	**0.0014**
CsCl	1.27	**0.0004**	0.0010	**0.0004**	0.0055	0.0005	0.0004	0.0005	0.0005	**0.0004**	**0.0003**	**0.0003**
		TDS wt %	11.08	TDS wt %	54.7	5.47	TDS wt %	6.24	5.61			

Bold → Analysed values from LA-ICP-MS or microthermometry; Bold underlined → adjusting values to fit measured element ratios and salinity in vapor (l)

Modeling procedure and assumptions following Landtwing et al. (2010, Table 2). Concentrations of intermediate density (ID) fluid inclusions in deep low Mo grade quartz-molybdenite vein (D50-2155) and concentrations of brine inclusions in boiling assemblage (BT2) in shallow high Mo grade quartz-molybdenite vein (JH2) were measured by LA-ICP-MS. Input fluid is based on average element ratios of all intermediate density fluid inclusions (column c). Element ratios and salinities of brine inclusions in boiling assemblage (column e) were adopted, whereas the poorly known salinities of intermediate density fluids, vapor and the mass fraction brine and vapor were varied to predict element ratios and salinity of vapor inclusions. The predicted element ratios were compared with analyzed element ratios (column l) to obtain an approximation satisfying all analytical constraints within their estimated uncertainty (Fig. 12). mMCl, mM, and gMCl molar mass of salt components, molar mass of elements, and weight (g) of salt components, respectively. Comp., pred, Conc., El-Ratio, and TDS represent composition, predicted value, concentration, element ratio, and total dissolved solids, respectively.

assemblages. By varying the fluid mass fractions of brine and salinity of the intermediate-density fluids, we predicted vapor salinities and element concentrations that match with the actually analyzed element ratios in the vapor inclusions, without generating negative concentration values (Table 6 and Fig. 12; c.f. Landtwing et al., 2010, Table 2 for procedure and assumptions). Results indicate that the deep single-phase fluid of the Mo stage separated into approximately 90% vapor and 10% brine by mass, although even higher vapor predominance (up to ~99%) is permitted by the compositional constraints. The fluid mass ratio of vapor/brine ~ 9:1 implies, based on the analyzed metal concentrations in the two boiling pairs (Seo et al., 2009; Fig. 11), that at least 70 % of the Mo in the deposit was precipitated from the vapor phase.

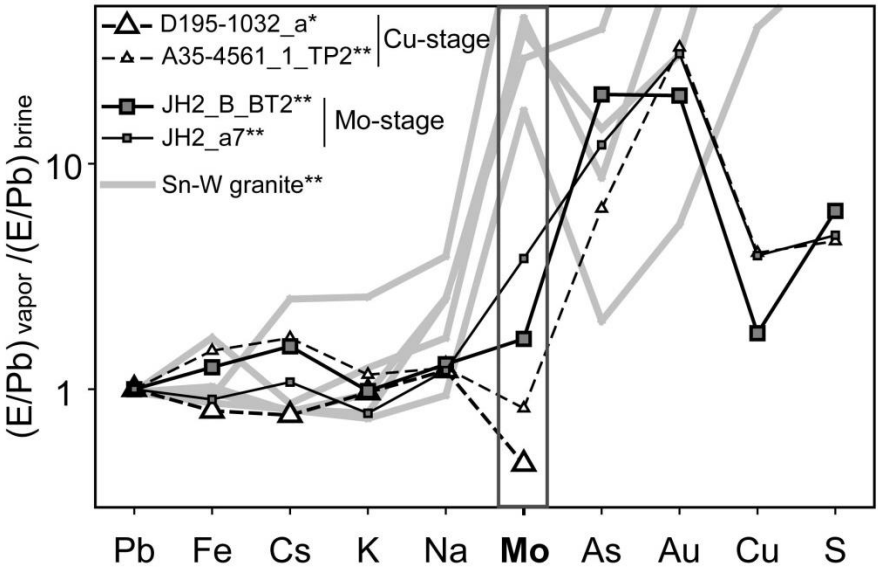

Figure 11. Elements ratios between coeval vapor and brine inclusions in cogenetic assemblages (boiling assemblage) in Cu-Au (D195-1032_a and A35-4561_1_TP2) and Mo-stages (JH2_B_BT2 and JH2_a7) in the Bingham Canyon deposit and the Sn-W-mineralized Mole Granite, including data from Landtwing et al. (2010) and Seo et al. (2009). Elements were normalized to Pb concentration (as an analytically more robust proxy for Cl and other chloride-complexed metals including Fe, Cs, Na; also K, Rb, Mn, Zn, Sr, Ba etc.), to show relative enrichment of S, As, Au ± Mo ± Cu in the vapor inclusions. Molybdenum is particularly enriched in vapor in the Sn-W granites (possibly due to more reduced and acidic fluid conditions) compared to the Bingham Canyon porphyry deposits. Among the fluid inclusion assemblages at Bingham Canyon, Mo partitioned more into the vapor during the Mo-stage than during the Cu-stage.

The greater concentration of the Mo ore shell towards the barren core (Fig. 1) and our microthermometric data indicate that fluids ascending during the Mo-stage started saturating molybdenite at somewhat higher pressure and temperature than the apparently quite restricted temperature window of Cu-Au deposition below 420°C (Landtwing et al., 2005). The fluid phase evolution (from intermediate-density to brine+vapor) as indicated by salinity constraints, width of solvus (Fig. 5), and mass balance of 9/1 ratios of vapor/brine remained essentially identical through both mineralization stages. These observations indicate that the P-T structure of the fluid plume was relatively stationary throughout the evolution from Cu-Au-stage to Mo-stage mineralization. This is consistent with recent geochronological evidence that all Cu-Au mineralization pulses occurred within a short but unresolved time interval of U-Pb zircon ages between 38.10 and 37.78 Ma (von Quadt et al., 2011), but is difficult to reconcile with Re-Os data suggesting that the Mo mineralization followed half a million years later at 37.00 ± 0.27 (Chesley and Ruiz, 1997).

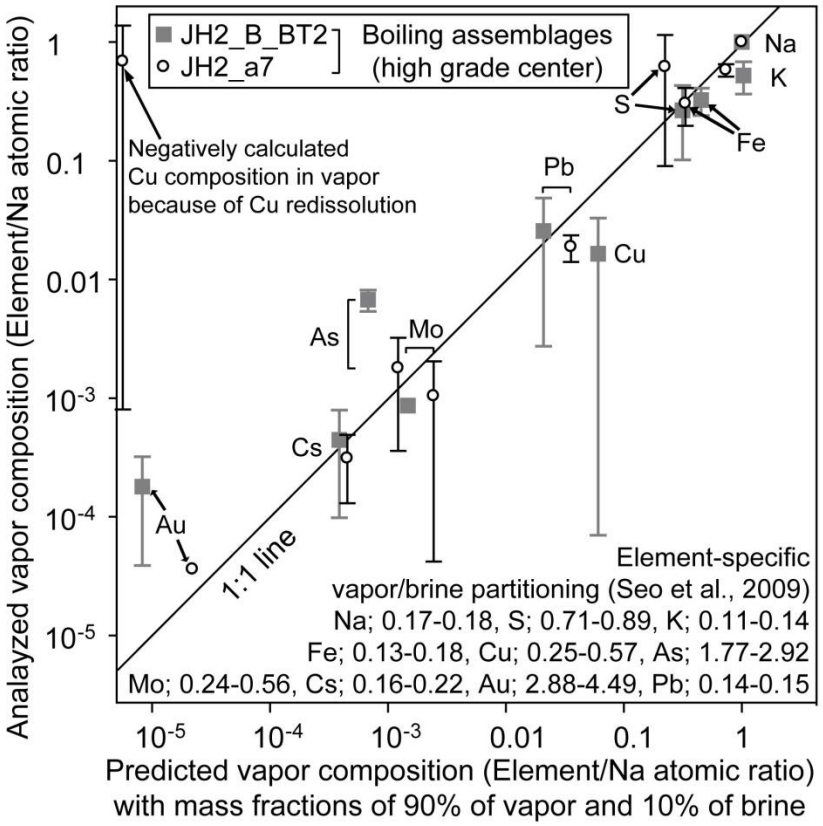

Figure 12. Comparison of best-estimate (mass balance prediction) vs. analyzed (LA-ICP-MS) vapor composition ratios during the Mo-stage. Mass proportions of ~ 90 % vapor and ~ 10 % brine are estimated based on the composition of intermediate-density fluid inclusions (low-grade Mo-stage sample D50-2155) and two boiling assemblages from a high grade quartz-molybdenite vein (B_BT2 and a7 in JH2). The calculation procedure is provided in the text and Table 6, following the approach of Landtwing et al. (2010) and including data from Seo et al. (2009).

Redox and pH affecting ore-metal precipitation

The precipitation of chalcopyrite, bornite, and molybdenite as major ore minerals in porphyry-style deposits depends on sulfide activity and requires an adequate quantity of sulfur in the hydrothermal fluids. Since the intermediate-density, brine, and vapor fluids contain enough S to precipitate all of their Cu and Mo as $CuFeS_2$ and MoS_2, the dominant ore minerals at Bingham Canyon (Figs. 7 and 8), a relatively small temporal change in redox conditions and acid balance within the magmatic fluid source may be responsible for large-scale metal separation by selective sulfide precipitation.

The stoichiometry of Cu and Mo sulfide precipitation reactions shows that a reduction of redox potential (lower fO_2) and an increase in the acidity (lower pH) in the hydrothermal fluids entering the Bingham Canyon deposit have opposing effects on the saturation of chalcopyrite and molybdenite, and may therefore trigger a switch from the first stage of predominant Cu-Fe-sulfide ± Au deposition to a second stage of preferential precipitation of molybdenite.

Chemical reactions for chalcopyrite precipitation from vapor-like fluids are likely to involve Cu(I)-S complexes such as $Cu(HS)_2^-$ and $Cu(HS)(H_2S)$ (Pokrovski et al., 2008; Seo et al., 2009; Etschmann et al., 2010):

$$2Cu(HS)_2^- + 2FeCl_{2(aq)} \rightarrow 2CuFeS_2 + 2Cl^- + 2HCl_{(aq)} + H_{2(aq)} \quad (1)$$

$$2Cu(HS)(H_2S)_{(aq)} + 2FeCl_{2(aq)} \rightarrow 2CuFeS_2 + 4HCl_{(aq)} + H_{2(aq)} \quad (2)$$

whereas deposition from the volumetrically minor brine phase probably includes chloride-complexed Cu(I) (Crerar and Barnes, 1976; Mountain and Seward, 1999, 2003).

$$CuCl_{(aq)} + FeCl_{2(aq)} + 2\,H_2S_{(aq)} \rightarrow CuFeS_2 + 3HCl_{(aq)} + 0.5\,H_{2(aq)} \quad (3)$$

All these reactions show that chalcopyrite saturation is promoted by oxidized fluid conditions (low H_2) and low acidity (low HCl concentration, i.e. more neutral pH).
Possible reactions for $Mo(IV)S_2$ precipitation can be formulated by using previously suggested Mo(VI) complexes in high-temperature hydrothermal fluids (Candela and Holland, 1984; Rempel et al., 2008; Ulrich and Mavrogenes, 2008; Rempel et al., 2009; Minubayeva and Seward, 2010).

$$MoO_{3(aq)} + H_{2(aq)} + 2H_2S_{(aq)} \rightarrow MoS_2 + 3H_2O \quad (4)$$
$$MoO_4^{2-} + 2H^+ + H_{2(aq)} + 2H_2S_{(aq)} \rightarrow MoS_2 + 4H_2O \quad (5)$$
$$HMoO_4^- + H^+ + H_{2(aq)} + 2H_2S_{(aq)} \rightarrow MoS_2 + 4H_2O \quad (6)$$
$$H_2MoO_{4(aq)} + H_{2(aq)} + 2H_2S_{(aq)} \rightarrow MoS_2 + 4H_2O \quad (7)$$
$$MoO_2Cl^+ + H_{2(aq)} + HS^- + H_2S_{(aq)} \rightarrow MoS_2 + 2H_2O + HCl_{(aq)} \quad (8)$$
$$MoO_2Cl_{2(aq)} + H_{2(aq)} + 2H_2S_{(aq)} \rightarrow MoS_2 + 2H_2O + 2HCl_{(aq)} \quad (9)$$
$$MoO_2Cl_3^- + H_{2(aq)} + 2H_2S_{(aq)} \rightarrow MoS_2 + 2H_2O + 2HCl_{(aq)} + Cl^- \quad (10)$$

To precipitate MoS_2 from oxy, hydroxy or oxy-chloride complexes of Mo(VI) will always require H_2S and H_2 (reactions 4-10). The solubility equilibria thus indicate that high H_2S activities and net reduction will favor molybdenite precipitations (Einaudi et al., 2003; Seedorff and Einaudi, 2004b). In the case of oxy- and hydroxy species, the reactions are either H^+-independent (4, 7) or consume acidity (5, 6). These molybdate species are likely to predominate in vapor-dominated systems in which Mo preferentially partitions into the vapor phase (Fig. 11), but a similar redox (and pH) dependence also applies if chloro-complexes were contributing to Mo transport.
Based on these contrasting effects of redox and pH on Cu and Mo precipitation reactions, we propose that a small difference in redox potential and acidity level in the mineralizing fluid may tip the balance of metal competition for a limited amount of sulfide in solution. If input fluid conditions during the early Cu-Au stage were relatively oxidizing (i.e. log fO_2 of about NNO+1; Audétat and Pettke, 2006) and alkaline, the saturation of MoS_2 upon cooling may have been retarded, allowing Cu-Fe sulfides to saturate first (reactions 1-3). If Cu and S concentrations are similar initially, the precipitation of Cu-Fe sulfide would rapidly deplete the S concentration in the fluid, preventing molybdenite precipitation even at lower temperature (Fig. 13A). As a consequence, the Mo advected by the fluids during the Cu-stage would be flushed out into the lithocap or into groundwater above the present erosion level (Williams-Jones and Heinrich, 2005; Arnorsson and Oskarsson, 2007), or be precipitated outside the porphyry-style orebody where the fluids met a S-rich reducing environment. Conversely, slightly more reducing conditions for the Mo-stage fluid may allow molybdenite to saturate first upon cooling, leading to effective MoS_2 deposition from an H_2S-rich fluid (reactions 4-10), followed by chalcopyrite saturation at slightly lower temperatures because of the more reducing and acidic conditions (reactions 1-3) and the lower initial Cu concentrations at similar S level (Fig. 13B).
The combined chemical effects of changes in redox and pH together with a steep temperature and pressure dependence in metal solubility are consistent with the mine scale distribution and the textural occurrences of chalcopyrite and molybdenite. Maximum Mo ore grades are displaced down and inward relative to the Cu ore shell (Fig. 1), consistent

with initial high-temperature saturation of molybdenite during the Mo-stage. Since Mo will never consume all S, and since even the Mo-stage fluid contained Cu in excess of Mo, it will eventually saturate Cu-Fe sulfide at somewhat lower temperature (Fig. 13B). This is consistent with the observation that molybdenite commonly precipitated as the first mineral, directly on the walls of the Mo stage veins, and was followed later by chalcopyrite in the central vug space of quartz-molybdenite veins (Fig. 2). Some of the late Cu introduced during the Mo-stage may also contribute to the Cu-Fe sulfides that are now hosted in texturally late positions in earlier quartz stockwork veins. This would have led to a cryptic upgrading of the Cu ore shell surrounding the zone of greatest Mo enrichment.

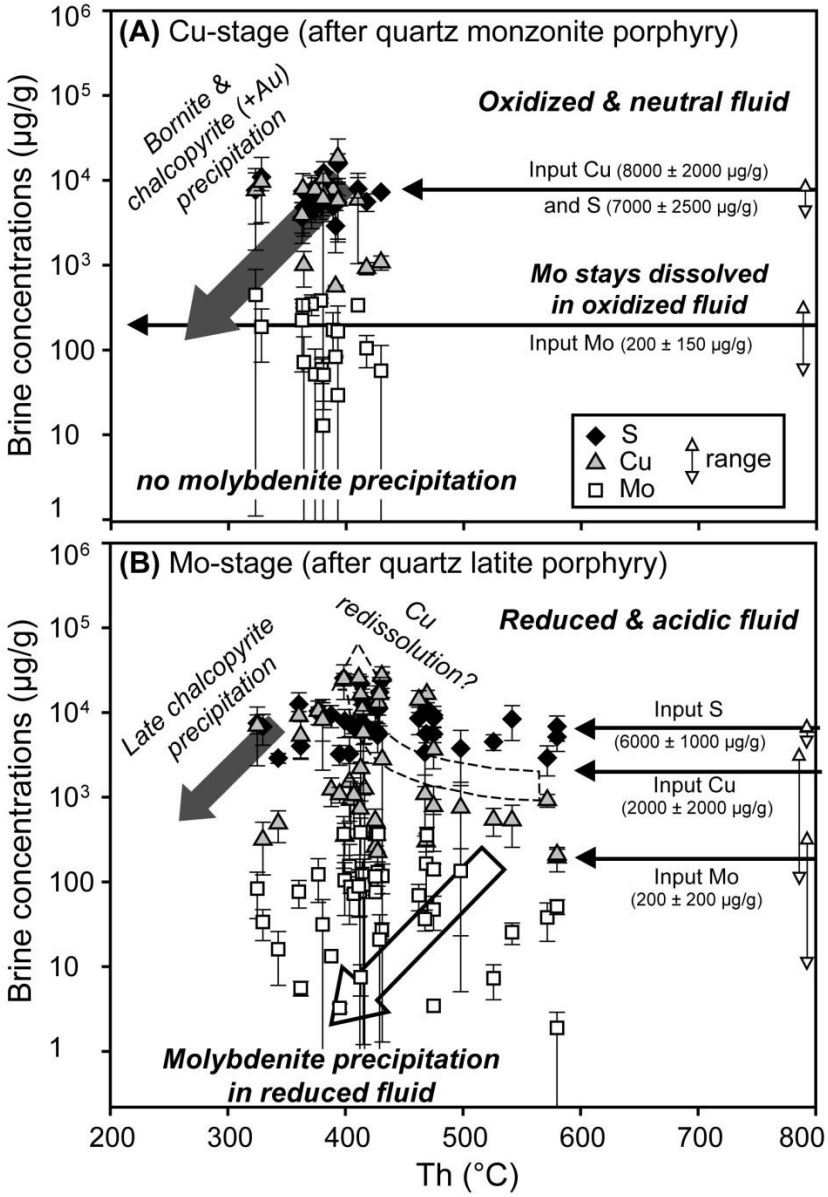

Figure 13. Sulfur, Cu, and Mo concentrations in brine inclusions and interpreted mechanisms responsible for the selective precipitations of Cu-Fe sulfide during the early Cu-stage (**A**) and molybdenite precipitation during the late Mo-stage (**B**) During the Cu-stage, relatively oxidized and neutral fluids are inferred to have exclusively precipitated Cu-Fe sulfides and Au, whereas Mo stayed dissolved in S-depleted fluids. During the Mo-stage, relatively reduced and acidic fluids favored molybdenite precipitation. Copper sulfide re-dissolution (Fig. 10) might have led to precipitation of late euhedral chalcopyrite in the vein center of quartz-molybdenite veins (see Fig. 2).

Independent evidence for a change towards more reducing and acid conditions from the early Cu-Au to the later Mo stage is weak, in light of the simple and non-diagnostic vein mineralogy, but permissive. Higher fluid acidity in the Mo-stage is indicated by the occurrence of feldspar-destructive alteration haloes, despite high temperature, along quartz-molybdenite veins, especially where a massive molybdenite seam directly overgrows the vein wall (Fig. 2B and 2C). The maximum value of the CH_4/CO_2 molar ratios in vapor inclusions, determined by the detection limit of Raman spectroscopy, corresponds to a minimum log fO_2 near NNO+0.3, based on the estimation by Ohmoto and Kendrick (1977) that S-type granitoids with a magmatic redox potential near FMQ≈NNO-1 yield hydrothermal fluids with a CH_4/CO_2 ratio near unity (note that the CH_4 to CO_2 oxidation reaction involves $2O_2$). In reality, the fluids may have been more reduced (higher CH_4) if the inclusions had lost H_2 by post-entrapment diffusional reequilibration, which would be consistent with chalcopyrite and anhydrite daughter crystals that do not dissolved during heating (Mavrogenes and Bodnar, 1994; Fig. 6). Elevated Fe/Mn ratios in brine inclusions of low-grade Mo-stage samples, compared to lower Fe/Mn ratios Cu-stage fluids (Fig. 9) are consistent with an evolution towards more reducing conditions in rock-buffered hydrothermal systems (Boctor, 1985), although it is not possible to quantify this trend for magmatic-hydrothermal conditions.

The proposed explanation for metal separation into distinct Cu-Au and Mo precipitation stages requires an evolution in the magmatic fluid source beneath Bingham Canyon. Compared to other porphyry-Cu-Au deposits, the Bingham Canyon system is relatively reduced. This is indicated by the absence of anhydrite from all magmatic rocks and all generations of hydrothermal veins (Klemm et al., 2007; Chambefort et al., 2008) and the lack of hydrothermal magnetite in the barren core of the Bingham system (Arancibia and Clark, 1996; Ulrich and Heinrich, 2001). Molybdenum-rich magmatic sulfides in mafic dikes (Keith et al., 1997) and igneous sulfide minerals in enclaves of fresh monzonite intrusions (Core et al., 2006) are also consistent with relatively reducing magmatic conditions. The reduced nature of the sedimentary country rocks, and the derivation of the Bingham magmas from subcontinental lithospheric mantle that had been metasomatised during the Paleoproterozoic, possibly without direct influence of an oxidized oceanic slab (Pettke et al., 2010), may have both contributed to the relatively reduced nature of all Bingham magmas. Evolution over time of an initially mildly oxidized magma (Cu-Au stage) towards a more reduced magma could be driven by mixing with a new batch of relatively reduced magma or by assimilation of organic-rich sedimentary rocks into the magma chamber below the Bingham Stock. Igneous magnetite crystallization may also contribute to progressive reduction of a magma, by taking ferric iron out of the melts (Sun et al., 2004). Magnetite is an abundant mineral in the EM and probably also in the subjacent batholith, as indicated by a large positive magnetic anomaly (Bankey et al., 1998; Steinberger et al., in prep.).

Evidence of quartz and sulfide redissolution

The anomalously high but consistent concentrations of Cu and S in some fluid inclusion assemblages in the Mo-stage (Fig. 7, 8 and 10) are an expected consequence of local redissolution of copper sulfide initiated in the field of retrograde quartz solubility at 400-500 °C and 200-500 bar (Fournier, 1999). Since the Mo-stage quartz veins do not host significant copper sulfides, except for some euhedral chalcopyrite in the vein center, varying concentrations of Cu and S in the Mo-stage fluids probably do not reflect the direct Cu-sulfide precipitations, but rather indicate Cu sulfide redissolution.

Cathodoluminescence (CL) imaging shows quartz redissolution followed by precipitation of a second generation of quartz in Mo-stage veins (Fig. 4), similar to textures in the Cu-stage stockwork veins (Redmond et al., 2004; Landtwing et al., 2005; Landtwing et al., 2010).

Some aliquots of late fluid ascending during in the Mo-stage would have intersected earlier Cu-stage veins, where quartz dissolution would help liberate and redissolve Cu-sulfides into relatively reduced, acidic and perhaps locally higher-temperature Mo-stage fluids. Such redissolution may explain the anomalous enrichment of Cu and S in a few fluid inclusion assemblages trapped as secondary trails in the quartz of the Mo stage (Fig. 10). Cu-sulfide redissolution or redistribution has previously been proposed for the Butte (Brimhall, 1979) and El Teniente deposits (Klemm et al., 2007).

Post-entrapment modifications of quartz-hosted fluid inclusion by Cu diffusion

Experimental studies have shown that the amount of copper in quartz-hosted melt and fluid inclusions can be significantly modified by reequilibraton with surrounding hydrothermal fluids, by selective diffusional exchange of H^+,Li^+, Na^+, Cu^+ and Ag^+ through the quartz host (Li et al., 2009; Zajacz et al., 2009). Most recently, it was proposed that the initially trapped high S contents of magmatic-hydrothermal fluid inclusion might enhance their capability to later take up Cu from external hydrothermal fluids, by inward diffusion and internal precipitation of a Cu-sulfide crystal, to the extent that the activities of Cu^+, H^+, and H_2S are adjusted to a new chemical equilibrium at lower-temperatures (Lerchbaumer and Audétat, 2011). This post-entrapment process might influence the positive correlations of sulfur and copper concentrations, and the accentuation of 1:2 molar ratios of copper and sulfur in natural quartz-hosted fluid inclusions from many magmatic-hydrothermal ore deposits (Seo et al., 2009). This discovery casts some doubt on the quantification of the proportion of Cu deposited by vapor or brine during the Cu-Au stage of mineralization at Bingham Canyon, but it does not change the conclusions that vapor was the dominant fluid phase throughout the mineralization history (Landtwing et al., 2011; this study). Overestimation of Cu-concentrations due to post-entrapment diffusional exchange of small singly-charged cations will affect the metal competition for sulfur during selective Cu, Au and Mo precipitation, once Cu-Fe-sulfide solubility can be calculated based on future experimental-thermodynamic data. However, it would not negate our proposed mechanism for the separation of Cu-Fe-sulfide and molybdenite precipitation by changing redox and pH conditions, which is primarily based on analyzed S and Mo concentrations and reaction stoichiometry.

Concluding Remarks

Despite the clear separation of molybdenum mineralization from copper – gold mineralization in space and time, the fluids depositing the two distinct ore stages at Bingham Canyon are compositionally similar and follow a similar evolution path. Single-phase magmatic input fluids cooled and expanded into predominant vapor and a minor proportion of condensing brine, and the bulk of the metals were precipitated from the expanding vapor phase. Unless we have missed a distinct precursor fluid, the Mo-stage fluids were not significantly enriched in molybdenum and sulfur. We conclude that oxidized and relatively neutral fluid condition favor precipitation of as chalcopyrite or bornite in the early mineralization stage and initially suppressed molybdenite precipitation. Later-stage fluids may have been more reduced and acid, as a result of a still uncertain evolution of the magmatic fluid source, which could tip the balance and favor molybdenite to become the first-saturating sulfide phase.

Experimental thermodynamic data will be required to evaluate the proposed mechanism of Cu and Mo separation, but subtle differences in pH and redox balance could explain the temporal and spatial separation of Mo and Cu ± Au observed in many other porphyry ore systems, where the two metals commonly occur in distinct vein sets, but in variable proportion, time sequence and deposit-scale spatial zonation.

Acknowledgments

This manuscript benefited from constructive reviews by David Cooke, Jacob Hanley and Kirsten Rempel. We thank Larry Meinert for editorial handling. Support by geologists of Kennecott Utah Company, notably Kim Schroeder, during our fieldwork at the Bingham Canyon deposit is gratefully acknowledged. Constructive comments from John Dilles, Kim Schroeder and Geoff Ballantyne on earlier versions of this manuscript are greatly appreciated, and we thank Thomas Wagner, Markus Wälle, Hiroyasu Murakami and Andreas Audétat for discussions about analytical work and geochemical interpretation. We also thank Marion Louvel and Glenn Lambrecht for assistance with Raman analyses at ETH Zurich and University of Bern. This study is funded by Swiss NSF Grants 200020-124906 and 200020-116693/1.

REFERENCES

Arancibia, O.N., and Clark, A.H., 1996, Early magnetite-amphibole-plagioclase alteration-mineralization in the Island Copper porphyry copper-gold-molybdenum deposit, British Columbia: ECONOMIC GEOLOGY, v. 91, p. 402-438.

Arnorsson, S., and Oskarsson, N., 2007, Molybdenum and tungsten in volcanic rocks and in surface and < 100 ^{0}C ground waters in Iceland: Geochimica et Cosmochimica Acta, v. 71, p. 284-304.

Audétat, A., and Pettke, T., 2006, Evolution of a porphyry-Cu mineralized magma system at Santa Rita, New Mexico (USA): Journal of Petrology, v. 47, p. 2021-2046.

Audétat, A., 2010, Source and evolution of molybdenum in the porphyry Mo(-Nb) deposit at Cave Peak, Texas Journal of Petrology, v. 51, p. 1739-1760.

Audétat, A., and Pettke, T., 2003, The magmatic-hydrothermal evolution of two barren granites: A melt and fluid inclusion study of the Rito del Medio and Canada Pinabete plutons in northern New Mexico (USA): Geochimica et Cosmochimica Acta, v. 67, p. 97-121.

Bankey, V., Grauch, T., and Kucks, R.P., 1998, Utah aeromagnetic and gravity maps and data, US Geological Survey Open-File Report, 98-761, US Geological Survey.

Beane, R.E., and Titley, S.R., 1981, Porphyry copper deposit; part II. Hydrothermal alteration and mineralization: ECONOMIC GEOLOGY 75th ANNIVERSARY VOLUME, p. 235-269.

Bingen, B., and Stein, H., 2003, Molybdenite Re-Os dating of biotite dehydration melting in the Rogaland high-temperature granulites, S Norway: Earth and Planetary Science Letters, v. 208, p. 181-195.

Boctor, N.Z., 1985, Rhodonite solubility and thermodynamic properties of aqueous $MnCl_2$ in the system MnO-SiO_2-HCl-H_2O: Geochimica et Cosmochimica Acta, v. 49, p. 565-575.

Bodnar, R.J., and Vityk, M.O., 1994, Interpretation of Microthermometric data for H_2O-NaCl fluid inclusions: Blacksburg, VirginiaTech, 117-130 p.

Brimhall, G.H., 1979, Lithologic determination of mass-transfer mechanisms of multiple-stage porphyry copper mineralization at Butte, Montana - vein formation by hypogene leaching and enrichment of potassium-silicate protore: ECONOMIC GEOLOGY, v. 74, p. 556-589.

Burke, E.A.J., 2001, Raman microspectrometry of fluid inclusions: Lithos, v. 55, p. 139-158.

Candela, P.A., and Holland, H.D., 1984, The partitioning of copper and molybdenum between silicate melts and aqueous fluids: Geochimica et Cosmochimica Acta, v. 48, p. 373-380.

Cao, X., 1989, Soulubility of molybdenite and the transport of molybdenum in hydrithermal solutions, PhD thesis, Iowa State University, USA.

Chambefort, I., Dilles, J.H., and Kent, A.J.R., 2008, Anhydrite-bearing andesite and dacite as a source for sulfur in magmatic-hydrothermal mineral deposits: Geology, v. 36, p. 719-722.

Chesley, J.T., and Ruiz, J., 1997, Preliminary Re-Os dating on molybdenite mineralization from the Bungham Canyon porphyry copper deposit, Utah, *in* John, D.A., and Ballantyne, G.H., eds., Geology and Ore Deposits of the Oquirrh and Wasatch Mountains, Utah, 29. Guidebook Series of the Society of Economic Geologists, p. 165-169.

Core, D.P., Kesler, S.E., and Essene, E.J., 2006, Unusually Cu-rich magmas associated with giant porphyry copper deposits: Evidence from Bingham, Utah: Geology, v. 34, p. 41-44.

Cox, D.P., and Singer, D.A., 1988, Distribution of gold in porphyry copper deposits: U.S. Geological Survey Open File Report, p. 88-46.

Crerar, D.A., and Barnes, H.L., 1976, Ore solution chemistry 5. Solubilities of chalcopyrite and chlcocite assemblages in hydrothermal solution at 200 ^{o}C to 350 ^{o}C: ECONOMIC GEOLOGY, v. 71, p. 772-794.

Driesner, T., and Heinrich, C.A., 2007, The system H_2O-NaCl. Part I: Correlation formulae for phase relations in temperature-pressure-composition space from 0 to 1000 ^{0}C, 0 to 5000 bar, and 0 to 1 X-NaCl: Geochimica et Cosmochimica Acta, v. 71, p. 4880-4901.

Einaudi, M.T., Hedenquist, J.W., and Inan, E.E., 2003, Sulfidation state of fluids in active and extinct hydrothermal system: Transition from porphyry to ephithermal environments: Society of Economic Geologist Special Publication 10, p. 285-313.

Etschmann, B.E., Liu, W., Testemale, D., Müller, H., Rae, N.A., Proux, O., Hazemann, J.L., and Brugger, J., 2010, An in situ XAS study of copper(I) transport as hydrosulfide complexes in hydrothermal solutions (25–592 °C, 180–600 bar): Speciation and solubility in vapor and liquid phases: Geochimica et Cosmochimica Acta, v. 74, p. 4723-4739.

Fournier, R.O., 1999, Hydrothermal processes related to movement of fluid from plastic into brittle rock in the magmatic-epithermal environment: ECONOMIC GEOLOGY, v. 94, p. 1193-1211.

Günther, D., Audétat, A., Frischknecht, R., and Heinrich, C.A., 1998, Quantitative analysis of major, minor and trace elements in fluid inclusions using laser ablation inductively coupled plasma mass spectrometry: Journal of Analytical Atomic Spectrometry, v. 13, p. 263-270.

Gruen, G., Heinrich, C.A., and Schroeder, K., 2010, The Bingham Canyon Porphyry Cu-Mo-Au Deposit. II. Vein geometry and ore shell formation by pressure-driven rock extension: ECONOMIC GEOLOGY, v. 105, p. 69-90.

Gu, Y., 1993, Theoretical and experimental studies of the hydrothermal geochemistry of molybdenum, PhD thesis, Monash University, Australia.

Guillong, M., and Heinrich, C.A., 2007, Sensitivity enhancement in laser ablation ICP-MS using small amounts of hydrogen in the carrier gas: Journal of Analytical Atomic Spectrometry, v. 22, p. 1488-1494.

Guillong, M., Latkoczy, C., Seo, J.H., Günther, D., and Heinrich, C.A., 2008a, Determination of sulfur in fluid inclusions by laser ablation ICP-MS: Journal of Analytical Atomic Spectrometry, v. 23, p. 1581-1589.

Guillong, M., Meier, D.L., Allan, M.M., Heinrich, C.A., and Yardley, B.W.D., 2008b, SILLS: A MATLAB-based program for the reduction of laser ablation ICP-MS data of homogeneous materials and inclusions: Mineralogical Association of Canada Short Course 40, p. 328-333.

Gustafson, L.B., and Hunt, J.P., 1975, Porphyry copper deposit at El-Salvador, Chile: ECONOMIC GEOLOGY, v. 70, p. 857.

Halter, W.E., Pettke, T., and Heinrich, C.A., 2002, The origin of Cu/Au ratios in porphyry-type ore deposits: Science, v. 296, p. 1844-1846.

Heinrich, C.A., 2006, From fluid inclusion microanalysis to large-scale hydrothermal mass transfer in the Earth's interior: Journal of Mineralogical and Petrological Sciences, v. 101, p. 110-117.

Heinrich, C.A., Driesner, T., Stefansson, A., and Seward, T.M., 2004, Magmatic vapor contraction and the transport of gold from the porphyry environment to epithermal ore deposits: Geology, v. 32, p. 761-764.

Heinrich, C.A., Pettke, T., Halter, W.E., Aigner-Torres, M., Audétat, A., Günther, D., Hattendorf, B., Bleiner, D., Guillong, M., and Horn, I., 2003, Quantitative multi-element analysis of minerals, fluid and melt inclusions by laser-ablation inductively-coupled-plasma mass-spectrometry: Geochimica et Cosmochimica Acta, v. 67, p. 3473-3497.

Keith, J.D., Whitney, J.A., Hattori, K., Ballantyne, G.H., Christiansen, E.H., Barr, D.L., Cannan, T.M., and Hook, C.J., 1997, The role of magmatic sulfides and mafic alkaline magmas in the Bingham and Tintic mining districts, Utah: Journal of Petrology, v. 38, p. 1679-1690.

Keppler, H., and Wyllie, P.J., 1991, Partitioning of Cu, Sn, Mo, W, U, and Th between melt and aqueous fluid in the systems halplogranite-H_2O HCl and halplogranite-H_2O HF Contributions to Mineralogy and Petrology, v. 109, p. 139-150.

Kesler, S.E., Chryssoulis, S.L., and Simon, G., 2002, Gold in porphyry copper deposits: its abundance and fate: Ore Geology Reviews, v. 21, p. 103-124.

Klemm, L.M., Pettke, T., and Heinrich, C.A., 2008, Fluid and source magma evolution of the Questa porphyry Mo deposit, New Mexico, USA: Mineralium Deposita, v. 43, p. 533-552.

Klemm, L.M., Pettke, T., Heinrich, C.A., and Campos, E., 2007, Hydrothermal evolution of the El Teniente deposit, Chile: Porphyry Cu-Mo ore deposition from low-salinity magmatic fluids: ECONOMIC GEOLOGY, v. 102, p. 1021-1045.

Landtwing, M.R., Furrer, C., Redmond, P.B., Pettke, T., Guillong, M., and Heinrich, C.A., 2010, The Bingham Canyon Porphyry Cu-Mo-Au Deposit. III. Zoned Copper-Gold Ore Deposition by Magmatic Vapor Expansion: Economic Geology, v. 105, p. 91-118.

Landtwing, M.R., Pettke, T., Halter, W.E., Heinrich, C.A., Redmond, P.B., Einaudi, M.T., and Kunze, K., 2005, Copper deposition during quartz dissolution by cooling magmatic-hydrothermal fluids: The Bingham porphyry: Earth and Planetary Science Letters, v. 235, p. 229-243.

Lerchbaumer, L., and Audétat, A., 2011, Preferential partitioning of copper into the vapor phase: fact or a natural artifact?: EGU General Assembly 201, Vienna, Austria, 2011, p. EGU2011-11906.

Li, Y., Audétat, A., Lerchbaumer, L., and Xiong, X.L., 2009, Rapid Na, Cu exchange between synthetic fluid inclusions and external aqueous solutions: evidence from LA-ICP-MS analysis: Geofluids, v. 9, p. 321-329.

Mavrogenes, J.A., and Bodnar, R.J., 1994, Hydrogen movement into and out of fluid inclusions in quartz - ExperImental evidence and geological implications: Geochimica et Cosmochimica Acta, v. 58, p. 141-148.

Minubayeva, Z., and Seward, T.M., 2010, Molybdic acid ionisation under hydrothermal conditions to 300 ◦C: Geochimica et Cosmochimica Acta, v. 74, p. 4365-4374.

Mountain, B.W., and Seward, T.M., 1999, The hydrosulphide sulphide complexes of copper(I): Experimental determination of stoichiometry and stability at 22 degrees C and reassessment of high temperature data: Geochimica et Cosmochimica Acta, v. 63, p. 11-29.

Mountain, B.W., and Seward, T.M., 2003, Hydrosulfide/sulfide complexes of copper(I): Experimental confirmation of the stoichiometry and stability of Cu(HS)(2)(-) to elevated temperatures: Geochimica et Cosmochimica Acta, v. 67, p. 3005-3014.

Murakami, H., Seo, J.H., and Heinrich, C.A., 2010, The relation between Cu/Au ratio and formation depth of porphyry-style Cu-Au +/- Mo deposits: Mineralium Deposita, v. 45, p. 11-21.

Ohmoto, H., and Kerrick, D., 1977, Devolatilization equilibria in graphitic systems: American Journal of Science, v. 277, p. 1013-1044.

Pettke, T., Oberli, F., and Heinrich, C.A., 2010, The magma and metal source of giant porphyry-type ore deposits, based on lead isotope microanalysis of individual fluid inclusions: Earth and Planetary Science Letters, v. 296, p. 267.

Pokrovski, G.S., Borisova, A.Y., and Harrichoury, J.C., 2008, The effect of sulfur on vapor-liquid fractionation of metals in hydrothermal systems: Earth and Planetary Science Letters, v. 266, p. 345-362.

Redmond, P.B., and Einaudi, M.T., 2010, The Bingham Canyon Porphyry Cu-Mo-Au Deposit. I. Sequence of Intrusions, Vein Formation, and Sulfide Deposition: ECONOMIC GEOLOGY, v. 105, p. 43-68.

Redmond, P.B., Einaudi, M.T., Inan, E.E., Landtwing, M.R., and Heinrich, C.A., 2004, Copper deposition by fluid cooling in intrusion-centered systems: New insights from the Bingham porphyry ore deposit, Utah: Geology, v. 32, p. 217-220.

Rempel, K.U., Migdisov, A.A., and Williams-Jones, A.E., 2006, The solubility and speciation of molybdenum in water vapour at elevated temperatures and pressures: Implications for ore genesis: Geochimica et Cosmochimica Acta, v. 70, p. 687-696.

Rempel, K.U., Williams-Jones, A.E., and Migdisov, A.A., 2008, The solubility of molybdenum dioxide and trioxide in HCl-bearing water vapour at 350 ^{0}C and pressures up to 160 bars: Geochimica et Cosmochimica Acta, v. 72, p. 3074-3083.

Rempel, K.U., Williams-Jones, A.E., and Migdisov, A.A., 2009, The partitioning of molybdenum(VI) between aqueous liquid and vapour at temperatures up to 370 degrees C: Geochimica et Cosmochimica Acta, v. 73, p. 3381-3392.

Rusk, B.G., Reed, M.H., and Dilles, J.H., 2008, Fluid inclusion evidence for magmatic-hydrothermal fluid evolution in the porphyry copper-molybdenum deposit at Butte, Montana: ECONOMIC GEOLOGY, v. 103, p. 307-334.

Seedorff, E., and Einaudi, M.T., 2004a, Henderson porphyry molybdenum system, Colorado: I. Sequence and abundance of hydrothermal mineral assemblages, flow paths of evolving fluids, and evolutionary style: ECONOMIC GEOLOGY, v. 99, p. 3-37.

Seedorff, E., and Einaudi, M.T., 2004b, Henderson porphyry molybdenum system, Colorado: II. Decoupling of introduction and deposition of metals during geochemical evolution of hydrothermal fluids: ECONOMIC GEOLOGY, v. 99, p. 39-72.

Seo, J.H., Guillong, M., Aerts, M., Zajacz, Z., and Heinrich, C.A., 2011, Microanalysis of S, Cl, and Br in fluid inclusions by LA-ICP-MS: Chemical Geology, v. 284, p. 35-44.

Seo, J.H., Guillong, M., and Heinrich, C.A., 2009, The role of sulfur in the formation of magmatic-hydrothermal copper-gold deposits: Earth and Planetary Science Letters, v. 282, p. 323-328.

Sillitoe, R.H., 1997, Characteristics and controls of the largest porphyry copper-gold and epithermal gold deposits in the circum-Pacific region: Australian Journal of Earth Sciences, v. 44, p. 373-388.

Sillitoe, R.H., 2010, Porphyry Copper Systems: ECONOMIC GEOLOGY, v. 105, p. 3-41.

Simon, A.C., Pettke, T., Candela, P.A., Piccolli, P.M., and Heinrich, C.A., 2006, Copper partitioning in a melt-vapor-brine-magnetite-pyrrhotite assemblage: Geochimica et Cosmochimica Acta, v. 70, p. 5583-5600.

Simon, G., Kesler, S.E., Essene, E.J., and Chryssoulis, S.L., 2000, Gold in porphyry copper deposits: Experimental determination of the distribution of gold in the Cu-Fe-S system at 400 ^{o}C to 700 ^{o}C: ECONOMIC GEOLOGY, v. 95, p. 259-270.

Singer, D.A., Berger, V.I., and Moring, B.C., 2005, Porphyry copper deposits of the world: database, map, and grade and tonnage models., US Geological Survey Open-File Report, US Geological Survey, p. 1060.

Steinberger, I., Hinks, D., Driesner, T., and Heinrich, C.A., in prep., The Bingham Canyon Porphyry Cu-Mo-Au) Deposit. V. Dimensions of a subjacent source intrusion based on geomagnetic and geochemical constraints.: ECONOMIC GEOLOGY.

Sun, W.D., Arculus, R.J., Kamenetsky, V.S., and Binns, R.A., 2004, Release of gold-bearing fluids in convergent margin magmas prompted by magnetite crystallization: Nature, v. 431, p. 975-978.

Ulrich, T., Günther, D., and Heinrich, C.A., 1999, Gold concentrations of magmatic brines and the metal budget of porphyry copper deposits: Nature, v. 399, p. 676-679.

Ulrich, T., and Heinrich, C.A., 2001, Geology and alteration geochemistry of the porphyry Cu-Au deposit at Bajo de la Alumbrera, Argentina: ECONOMIC GEOLOGY, v. 96, p. 1719-1742.

Ulrich, T., and Mavrogenes, J., 2008, An experimental study of the solubility of molybdenum in H_2O and KCl-H_2O solutions from 500 ^{0}C to 800 ^{0}C, and 150 to 300 MPa: Geochimica et Cosmochimica Acta, v. 72, p. 2316-2330.

von Quadt, A., Erni, M., Martinek, K., Moll, M., Peytcheva, I., and Heinrich, C.A., 2011, Zircon crystallization and the life times of ore-forming magmatic-hydrothermal systems: Geology, v. 39, p. 731-734.

Wallace, S.R., 1995, Presidental address; The Climax-type molybdenite deposits - What they are, Where they are, and Why they are.: Economic Geology and the Bulletin of the Society of Economic Geologists, v. 90, p. 1359-1380.

White, W.H., Bookstrom, A.A., Kamilli, R.J., Ganster, M.W., Smith, R.P., Ranta, D.E., and Steininger, R.C., 1981, Character and origin of Climax-type molybdenum deposits: ECONOMIC GEOLOGY, v. 75th Anniversary Volume, p. 270-316.

Williams-Jones, A.E., and Heinrich, C.A., 2005, Vapor transport of metals and the formation of magmatic-hydrothermal ore deposits: ECONOMIC GEOLOGY, v. 100, p. 1287-1312.

Wood, S.A., Crerar, D.A., and Borcsik, M.P., 1987, Solubility of the assemblage pyrite-pyrrhotite-magnetite-sphalerite-galena-gold-stibnite-bismuthinite-argentite-molybdenite in H_2O-NaCl-CO_2 solutions from 200 ^{o}C to 350 ^{o}C: ECONOMIC GEOLOGY, v. 82, p. 1864-1887.

Zajacz, Z., and Halter, W., 2009, Copper transport by high temperature, sulfur-rich magmatic vapor: Evidence from silicate melt and vapor inclusions in a basaltic andesite from the Villarrica volcano (Chile): Earth and Planetary Science Letters, v. 282, p. 115-121.

Zajacz, Z., Hanley, J.J., Heinrich, C.A., Halter, W.E., and Guillong, M., 2009, Diffusive reequilibration of quartz-hosted silicate melt and fluid inclusions: Are all metal concentrations unmodified?: Geochimica et Cosmochimica Acta, v. 73, p. 3013-3027.

Zajacz, Z., Seo, J.H., Candela, P.A., Piccoli, P.M., Heinrich, C.A., and Guillong, M., 2010, Alkali metals control the release of gold from volatile-rich magmas: Earth and Planetary Science Letters, v. 297, p. 50-56.

Table Captions

Table 1. Descriptions of the quartz vein samples from drill core and mine outcrops that were used for fluid inclusion analyses.

EM = equigranular monzonite, QMP = quartz monzonite porphyry, QLP = quartz latite porphyry.

Table 2. Composition of Cu-stage (quartz stockwork veins) brine inclusion assemblages in the Bingham Canyon deposit.

Averages (Av.; µg/g) and standard deviations (SD; 1 sigma) of elements in Cu-stage (quartz stockwork veins). Salinities (Sal.; equivalent NaCl wt %) and homogenization temperatures (T_h) of the assemblages were obtained from microthermometry (Bodnar and Vityk, 1994) and pressures of entrapment were estimated (Driesner and Heinrich, 2007). "Deep stw.", "Cu-vein", and "QLP stw" represent low Cu grade quartz stockwork veins, high Cu grade quartz stockwork vein, and late-stage (post-QLP) quartz stockwork vein, respectively. Boiling assemblages "boil" allow direct calculation "real PT" of pressures, whereas brine-only "no-boil" assemblages provide minimum estimation "min PT" of pressures. "ND" represents values not determined.

Table 3. Composition of Mo-stage (quartz-molybdenite veins) brine inclusion assemblages

"deep moly", and "Mo-vein" represent low grade quartz-molybdenite veins, and high grade quartz-molybdenite veins, respectively.

Table 4. Concentration of additional elements (Mn, Rb, Sr, Ba) in brine inclusion assemblages in low-grade veins from barren core Cu-stage and Mo-stage in Bingham Canyon deposit.

"Deep stw." and "Deep Moly" represent quartz stockwork veins with low Cu grade and low grade quartz-molybdenite veins, respectively. For the element ratio determinations, we assumed 3,000 µg/g of Pb as an internal standard and used analytically-robust Fe/Mn ppm ratios.

Table 5. Compostion of intermediate-density (ID), vapor, and late aqueous fluid inclusion assemblages.

Due to difficulties to get reliable salinities from such low-density fluid inclusions, most of the intermediate-density (ID) and vapor phase salinities were assumed as 8 equiv. NaCl wt % based on previous estimations (Redmond et al., 2004; Landtwing et al., 2010). Only element ratios are analytically-robust and are therefore reported in the current text. Temperatures, pressure data for some vapor inclusions were obtained from brine inclusion data in boiling assemblages.

Table 6. Mass-balance calculation to estimate vapor composition and vapor-brine mass fractions.

Modeling procedure and assumptions following Landtwing et al. (2010, Table 2). Concentrations of intermediate-density (ID) fluid inclusions in deep low Mo grade quartz-molybdenite vein (D50-2155) and concentrations of brine inclusions in boiling assemblage (BT2) in the shallow high Mo grade quartz-molybdenite vein (JH2) were measured by LA-ICP-MS. Input fluid is based on average element ratios of all intermediate-density fluid inclusions (column c). Element ratios and salinities of brine inclusions in boiling assemblage (column e) were adopted, whereas the poorly known salinities of intermediate-density fluids, vapor and the mass fraction brine and vapor were varied to predict element ratios and salinity of vapor inclusions. The predicted element ratios were compared with analyzed element ratios (column l) to obtain an approximation satisfying all analytical constraints within their estimated uncertainty (Fig. 12). mMCl, mM, and gMCl molar mass of salt components, molar mass of elements, and weight (g) of salt components, respectively. Comp., pred, Conc.,

El-Ratio, and TDS represent composition, predicted value, concentration, element ratio, and total dissolved solids, respectively.

Figure Captions

Figure 1.

Figure 2.

Figure 3.

Figure 4.

Figure 5.

Figure 6.

Figure 7.

Figure 8.

Figure 9.

Figure 10.

Figure 11.

Figure 12.

Figure 13.